

Research on advanced signal processing in a white-light
scanning interferometer for exact measurements of
surface profile and film thickness

Doctoral Program of Electrical and Information Engineering
Graduate School of Science and Technology
Niigata University

LUO Songjie

August 2019

ABSTRACT

The white-light scanning interferometry is a kind of the three-dimensional measurement technology for surface profile and thickness of thin film. Because of the features of large measurement range, fast measurement speed, non-invasive and high precision, the white-light scanning interferometry becomes a preferable technology to measure the surface profile and the thickness of thin film. However the dispersion phase caused by the changing refractive index of optical components with different wavelengths in white-light scanning interferometers makes the measured optical path difference (OPD) of zero imprecise. The random noise generated by the vibration also makes the OPD instable. In order to eliminate these disturbances, a serial of research are proposed to improve the measurement accuracy in this dissertation.

Main research and innovations of this dissertation are as follows:

(1) Utilization of complex-valued interference signal (CVIS) in white-light scanning interferometer (WLSI).

Fourier transform and inverse Fourier transform are performed on the white-light scanning interference signal to obtain the complex-valued interference signal. The zero phase position Z_p nearest the maximum amplitude position Z_a obtained from the complex-valued interference signal is proposed as the new measurement value.

(2) Dispersion phase elimination by using spectral analyzer.

The dispersion phase in WLSI is obtained from the real-valued interference signal detected by spectral resolved interferometer (SRI) through the Fourier transform. The dispersion phase in the SRI is subtracted from the spectral phase in Fourier transform of the CVIS of the WLSI. Through inverse Fourier transform of this spectral distribution, a dispersion-free CVIS is obtained, and the position Z_p provides a surface profile with an error less than 4 nm. The repeatability of three measurements in an interval of about 10 min is 1.2 nm.

(3) Dispersion phase elimination by using a least square line in spectral phase distribution.

Since the capture and process of the interference signal from SRI before the measurement of surface profile makes the experiment complicated, a new signal processing is proposed to eliminate the dispersion phase simply. After Fourier transform of interference signal in the WLSI, the spectral phase of interference signal is obtained in wavenumber domain. The linear and bias components in the spectral phase distribution are used to calculate the complex-valued interference signal (CVIS) by inverse Fourier transform. This signal processing without using a measured dispersion phase provide a surface profile with an error less than 4 nm. The repeatability is 1.3 nm

(4) Interference signal correction by detection of scanning position.

In order to obtain the surface profile with higher accuracy than the result obtained from research (3), it is necessary to eliminate the random vibration of optical

components and non-linear movement of PZT in the experiment. The actual OPD is detected with an additional interferometer in the WLSI by using an optical band-pass filter. The interference signal of the WLSI is corrected with the real OPD values or the real scanning position values. By this correction method, a surface profile with a step shape of 3- μm height is measured accurately with an error less than 2 nm. The repeatability is about 0.5 nm.

(5) Compensation of dispersion effect in shape measurement of thin glass plate.

In shape measurement of a thin glass plate the rear surface profile cannot be measured by the method of the research (3) because the dispersion effect exists in the glass plate. The position Z_p of amplitude maximum in the CVIS is not equal to the position of the rear surface. From simulation results it is made clear that the positions Z_a and Z_p are proportional to the rear surface position or the thickness of the glass plate. The proportional coefficients for Z_a and Z_p are determined to $C_a=1.53612$ and $C_p=1.51506$, respectively, by the simulations. By using the C_a and C_p , the errors of measured front and rear surface profile are less than 4 nm, and the measured thickness has an error less than 4 nm and the repeatability is 2.4 nm.

CONTENTS

ABSTRACT.....	I
CHAPTER 1 INTRODUCTION	1
1.1 Motivation.....	1
1.1.1 Single wavelength interferometry.....	2
1.1.2 White-light scanning interferometry.....	3
1.2 White-light scanning interferometer	3
1.2.1 Envelop peak and fringe peak in interference signal	3
1.2.2 Processing in scanning position domain	4
1.2.3 Processing in wavenumber domain	5
1.3 Innovations.....	6
CHAPTER 2 COMPLEX-VALUED INTERFERENCE SIGNAL IN WHITE-LIGHT SCANNING INTERFEROMETER	9
2.1 Theory	9
2.1.1 Interference signal detected in white-light scanning interferometer.....	9
2.1.2 Complex-valued interference signal	10
2.1.3 Measurement values of Z_a and Z_p	11
2.2 Conclusion	11
CHAPTER 3 DISPERSION PHASE ELIMINATION BY USING SPECTRAL ANALYZER	12
3.1 Introduction.....	12
3.2 Principle	12
3.2.1 Dispersion phase of beam-splitter.....	12
3.2.2 Spectral resolved interferometer	14
3.2.3 Elimination of dispersion phase.....	14
3.3 Experiment.....	15
3.3.1 Detection of dispersion phase	15
3.3.2 Signal acquisition and processing.....	18
3.4 Measurement result	21
3.5 Conclusion	24
CHAPTER 4 DISPERSION PHASE ELIMINATION BY USING A LEAST SQUARE LINE IN SPECTRAL PHASE DISTRIBUTION.....	26
4.1 Introduction.....	26
4.2 Principle	26
4.2.1 Least square line in spectral phase distribution	26
4.2.2 Relation between Z_a and Z_p	29
4.3 Simulation	30
4.3.1 Effect of dispersion phase on measurement accuracy	33
4.3.2 Effect of random noise on measurement accuracy	34
4.4 Experiment.....	35
4.5 Measurement result	37
4.6 Conclusion	39

CHAPTER 5 INTERFERENCE SIGNAL CORRECTION BY DETECTION OF SCANNING POSITION.....	41
5.1 Introduction.....	41
5.2 Principle.....	42
5.3 Detection of the scanning position and its components.....	45
5.4 Simulation of effect of different phase error.....	47
5.4.1 Effect of the non-linear movement of PZT.....	49
5.4.2 Effect of the random movement.....	49
5.4.3 Effect of the additive noise.....	50
5.5 Experiment.....	50
5.6 Measurement result.....	52
5.7 Conclusion.....	56
CHAPTER 6 COMPENSATION OF DISPERSION EFFECT IN SHAPE MEASUREMENT OF THIN GLASS PLATE.....	57
6.1 Introduction.....	57
6.2. Principle.....	57
6.2.1 Signals generated by front and rear surfaces.....	57
6.2.2. Characteristics of Z_{a2} and Z_{p2}	60
6.2.3. Calculation of thickness.....	61
6.3 Experiment.....	62
6.3.1 Setup of interferometer and detected signals.....	62
6.3.2 Signal processing.....	64
6.4 Experiment result.....	65
6.5 Conclusion.....	71
CHAPTER 7 CONCLUSIONS.....	72
REFERENCE.....	74
LIST OF PUBLICATION.....	78
ACKNOWLEDGEMENT.....	80

CHAPTER 1

INTRODUCTION

1.1 Motivation

Due to the development of precise processing technology, the structure on the surface profile of devices become more sophisticated. The optical components, micro circuitry and micro machineries require precise structure to guarantee the high performance. The surface profile and the thin film on the surface are very important factors to affect the quality of the product. However the product always has a more complex surface profile compared with the theoretical surface. The measurement of the surface profile and shape of thin film become more and more important to distinguish the character of the product.

Since the surface profile and the thin film of the product are always generated by the mechanical processing, corrosion, and coating, the manufacturing error of these technologies cause the defect of the product. For example, the deformation or tear of the surface is caused by the friction between the product and mechanics. The vibration of manufacturing system produces fluctuations on the surface. Thus the three-dimensional surface profile measurement method is necessary to show the entire characterization [1-2].

The three-dimensional surface profile measurement method can be classified as contact and non-contact measurement [3-16] depending on whether the surface of the object is touched or not. The stylus profilometry is the contact type measurement method with high precision. However the stylus will damage the surface structure if the tested object is soft, especially the surface is coated with aluminum or other soft metal. The wear of the probe also affects the measurement accuracy. And scanning point by point makes the measurement slowly. These weaknesses limit the application of the contact measurement method. In order to satisfy the three-dimensional measurement with high accuracy, fast speed and non-invasive, the non-contact method based on the optical principle becomes an important research direction.

Interferometry is a kind of non-contact measurement method to detect the surface profile by analyzing the interference signal generated by the reflected light from the reference surface and the object. It has the advantages of fast measurement speed, high accuracy and simply operation.

According to the kind of light source, there are single wavelength interferometer [17-23] and white-light interferometer.

1.1.1 Single wavelength interferometry

The single wavelength interferometry is investigated early. The Michelson interferometer is used to describe the theory of interferometry as shown in the Fig. 1.1. The principle of optical interferometry is analyzing the interference signal generated by the reflected light from the reference surface and the object. There is a step on the object whose height h is 20 nm. There are two measurement points A and B on the object surface. The intensity of interference signal changes with the movement of reference surface controlled by the piezoelectric transducer (PZT).

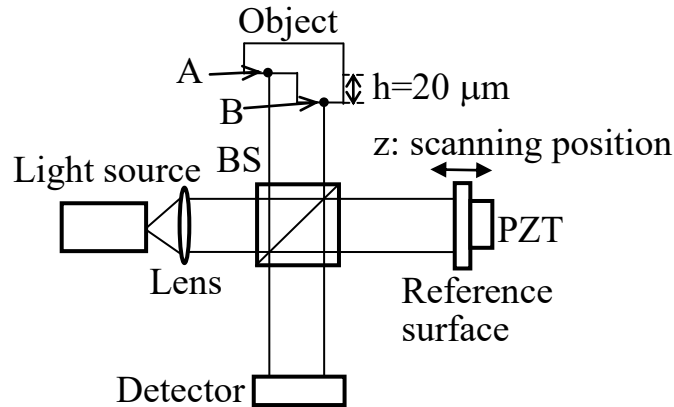


Fig. 1.1. The schematic of Michelson interferometer.

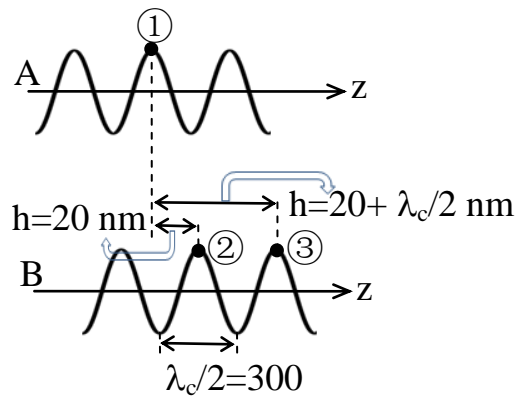


Fig. 1.2. The interference signal generated by single wavelength.

When the light source only has single wavelength λ_c in Fig. 1.1, the interference signal is shown in Fig. 1.2. The OPD of the position ① is zero in the interference signal generated by the measurement point A. The OPD of the position ② is zero in the interference signal generated by the measurement point B. The distance between the position ① and ② is 20 nm

which equal to the height of step on the object surface. If the $h=20+\lambda_c/2$ nm, the OPD of the position ③ is zero. However the interference signals B generated by $h=20$ nm and $h=20+\lambda_c/2$ nm are almost same. It is impossible to determine the exact value of h from the interference signals A and B. The measurement range of single wavelength interferometer must be less than $\lambda_c/2$.

1.1.2 White-light scanning interferometry

When the light source has multi-wavelength, there are many interference signals with different wavelengths $\lambda_1, \lambda_2, \lambda_3, \dots$ as shown in Fig. 1.3. After the summation of interference signals with different wavelengths, the white-light interference signal generated by point A and B are obtained. It is easy to find the position of OPD=0 from two white-light interference signals because of their decaying intensity. And the decaying intensity also prevents the selection of wrong maximum value affected by noise. Compared with the single wavelength interferometer, the measurement range of white-light scanning interferometer (WLSI) is determined by the scanning distance of reference surface. Therefore, the WLSI is investigated in this dissertation.

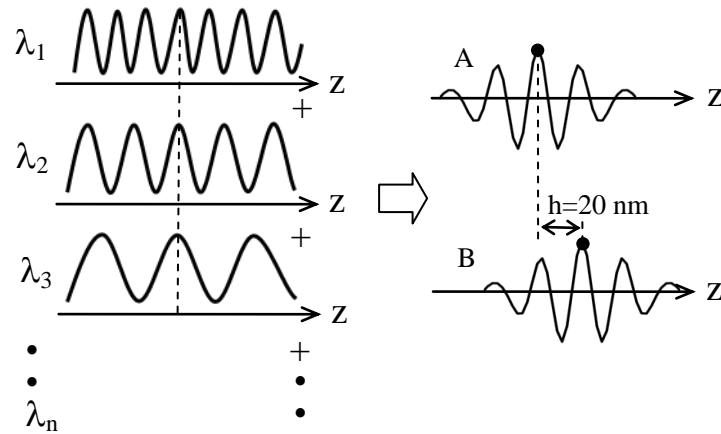


Fig. 1.3. The interference signal generated by multi-wavelength.

1.2 White-light scanning interferometer

1.2.1 Envelop peak and fringe peak in interference signal

The function of ideal interference signal in Fig. 1.4 is expressed as $S(z)=A(z)\cos[\varphi(z)]$, where the $A(z)$ is the amplitude or envelop and the $\varphi(z)$ is the phase. Z_o is the object position. The envelop peak Z_E is maximum position of $A(z)$. The fringe peak Z_F is maximum position of $S(z)$. The Z_E and Z_F are two conventional values to obtain the object position Z_o . The Z_F is calculated as [24-28]

$$Z_F = \frac{\sum S(z) * z}{\sum S(z)} \quad (1.1)$$

Fourier transform and Hilbert transform [35-36] are two common methods to obtain the envelop distribution [34-38] of the interference signal. The spectral distribution of $S(z)$ is obtained by the Fourier transform. Inverse Fourier transform is performed on the positive component of spectral distribution of $S(z)$ to obtain the complex-valued interference signal. The envelop distribution calculated by the square root of quadratic sum of real part and imaginary part of the complex-valued interference signal. When the Hilbert transform is performed on the interference signal, the new signal with the $\pi/2$ delay is obtained. The envelop distribution calculated by the square root of quadratic sum of original interference signal and new signal. Since the Fourier transform is used in the experiment, it will be explained detailed in chapter 2.

In ideal signal, the $Z_E=Z_F=Z_o$ proves that Z_E and Z_F provide exact measurement result in ideal interference signal. However the dispersion phase, random phase noise and not linear scanning cause the $Z_E \neq Z_F \neq Z_o$ in actual signal. It means that the Z_E and Z_F cannot provide the exact position of Z_o in experiment. From other research, the position of $\varphi(z)=0$ provides a more exact Z_o than Z_E and Z_F . Two methods are introduced to obtain the position of $\varphi(z)=0$ from actual signal.

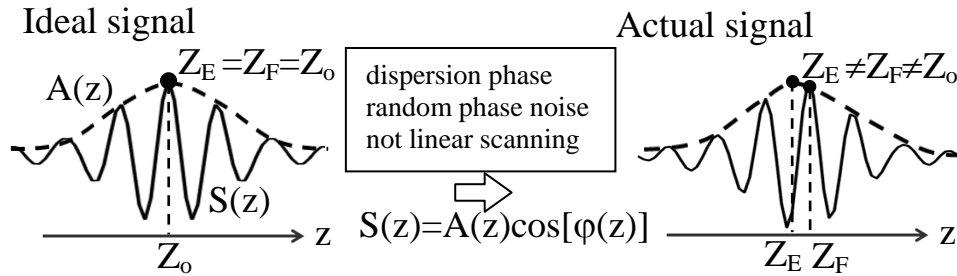


Fig. 1.4. Ideal and actual interference signals. $S(z)$ is the function of interference signal. Z_o is the object position. Z_E is maximum position of $A(z)$. Z_F is maximum position of $S(z)$.

1.2.2 Processing in scanning position domain

Phase-shifting method [29-33] is one of signal processing method in scanning position domain to obtain the position of $\varphi(z)=0$. It is developed from the phase-shifting method of single wavelength interference signal. Figure 1.5 shows the white-light scanning interference signal whose interval of intensity value is $\Delta\varphi$. The $\Delta\varphi$ is determined by the movement of PZT. According to the type of $\Delta\varphi$, there are two kinds of the phase-shifting methods. One is derived on the premise of the known $\Delta\varphi$ such as *Hariharan* phase-shifting algorithm. The other one has the constant and unknown $\Delta\varphi$

such as *Carre* phase-shifting algorithm. In the *Hariharan* five-step phase-shifting algorithm, the initial phase ϕ is obtained when $\Delta\phi=\pi/4$.

$$\phi=\arctan\left[\frac{2(I_2-I_4)}{2I_3-I_5-I_1}\right] \quad (1.2)$$

where the $I_1, I_2, I_3\dots$ are the intensity values of sampling points with constant $\Delta\phi$.

In the phase-shifting method, only a few intensity values are used to calculate the object position which makes the measurement fast. However the small amount of sampling points makes the measurement very sensitive to the displacement accuracy and noise.

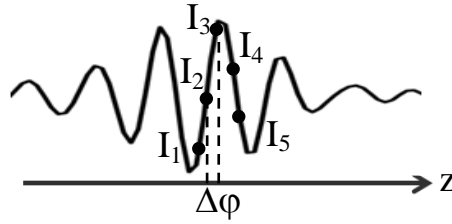


Fig. 1.5. Sampling points of white-light scanning interference signal with a constant interval $\Delta\phi$.

1.2.3 Processing in wavenumber domain

The other method to obtain the position of $\varphi(z)=0$ is the signal processing in wavenumber domain [39-41]. Figure 1.6 shows spectral distribution of white-light scanning interference signal obtained by Fourier transform. The horizontal axis is wavenumber $\sigma=1/\lambda$. The $I(\sigma)$ and $\varphi(\sigma)$ are amplitude and phase, respectively. The red line is the linear component obtained from $\varphi(\sigma)$ by the least square method. Denoting the slope of red line as a_1 and the index of averaged wavelength as n_G , the relatively change Δh of two measurement points is given

$$\Delta h = \frac{\Delta a_1}{4\pi n_G} \quad (1.3)$$

where the Δa_1 is the difference of slope of red line between two measurement points.

This method is not suitable when the big dispersion phase exist. The random noise is also an inevitable error.

The non-linear displacement of PZT and random noise [45-51] such as mechanical vibration has a bad influence on the white-light scanning interference signal. Since the refractive index of the material is relate to the wavelength, the broad spectrum brings the dispersion phase to the interference signal in the thickness measurement of the object [52-56].

Therefore new signal processing methods are proposed to decrease the influence of dispersion phase [42-44] and random noise [57].

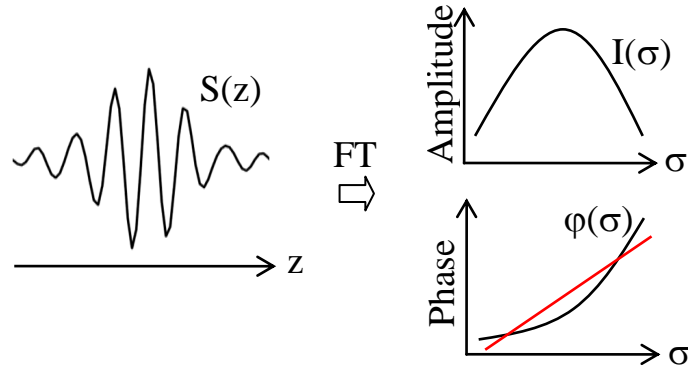


Fig. 1.6. Distribution of Fourier transformed white-light scanning interference signal. $I(\sigma)$ is amplitude and $\varphi(\sigma)$ is phase.

1.3 Innovations

This thesis describes fundamental knowledge related to the WLSIs and a serial of research to eliminate the dispersion phase and random noise.

The main sentences are as follows:

Chapter2: Complex-valued interference signal in white-light scanning interferometer.

Fourier transform and inverse Fourier transform are performed on the white-light scanning interference signal to obtain the complex-valued interference signal (CVIS). The maximum value of amplitude is denoted as the Z_a , and zero phase position nearest to Z_a is denoted as Z_p . The measurement value Z_p is proposed to measure the object position of Z_o .

Chapter 3: A method to eliminate dispersion phase in a WLSI by using a spectrally resolved interferometer (SRI).

The spectral resolved interferometer is Michelson interferometer with a broadband light source and spectral analyzer. The real-valued interference signal along the wavelength is detected by spectral analyzer. Complex-valued interference signals (CVISs) of a WLSI and a SRI are obtained from their real-valued interference signals through Fourier transform. The phase distribution in the CVIS of the SRI indicates a dispersion phase caused by two sides of unequal length in a cubic beam splitter, and the magnitude of the dispersion phase changes linearly along a horizontal direction of the beam splitter. The dispersion phase in the SRI is subtracted from the spectral phase in Fourier transform of the CVIS of the WLSI. Through inverse Fourier transform of this spectral distribution, a dispersion-free CVIS is obtained, and the position of zero phase nearest to the position of amplitude maximum provides a surface profile with an error

less than 4 nm. The repeatability of three measurements in an interval of about 10 min is 1.2 nm. A traditional method to obtain the surface profile by using the slope of phase of Fourier transform of the CVIS of the WLSI is carried out to compare the result. The surface profile obtained by the traditional method has an error less than 12 nm and the repeatability is 13.2 nm. It is clear that the utilization of the CVIS of the WLSI and SRI allows achieving highly accurate measurements of surface profile.

Chapter 4: A new signal processing method to obtain exact surface profile measurement without subtracting dispersion phase.

Since the capture and process of the interference signal from SRI before the measurement of surface profile makes the experiment complicated, a new signal processing is proposed to eliminate the dispersion phase simply. After Fourier transform of interference signal in the WLSI, the spectral phase of interference signal is obtained in wavenumber domain. The linear and bias components in the spectral phase distribution are used to calculate the complex-valued interference signal (CVIS) by inverse Fourier transform. The simulations verify that the dispersion phase generates an inclination in the measured surface profile along one direction in which the magnitude of the dispersion phase changes linearly. The simulations also show that the position of zero phase nearest the position of amplitude maximum in the CVIS almost does not change due to the bias component, although the random phase noise contained in the interference signal changes the slope of the linear component. This signal processing without using a measured dispersion phase provides a surface profile with an error less than 4 nm. The repeatability is 1.3 nm. Measured surface profiles show that the new signal processing achieves highly accurate measurement by the CVIS.

Chapter 5: A signal correction method to correct the scanning position errors in a WLSI.

In order to obtain the surface profile with higher accuracy than the result obtained from chapter 4, it is necessary to eliminate the noise in the experiment. Since the scanning position of PZT in WLSI contains error of the random vibration of optical components and non-linear movement of PZT, an actual optical path difference (OPD) between the object and reference beams changing with time is detected with an additional interferometer in which the two beams interfering with each other of in the WLSI and an optical band-pass filter are used. This interferometer is simply equipped in the WLSI and does not give a bad effect to the WLSI. The real OPD same as that in the WLSI is easily calculated from the interference signal of the additional interferometer by the same signal processing used in the WLSI. The interference signal of the WLSI is corrected with the real OPD values or the real scanning position values. The corrected interference signal with a constant sampling interval is obtained with an interpolation method. By this correction method, a surface profile with a step shape of 3- μm height is measured accurately with an error less than 2 nm. The

repeatability is about 0.5 nm. It is clear that the correction method can provide higher measurement accuracy than the method in chapter 4.

Chapter 6: A method to measure the shape of thin glass plate by considering dispersion effects.

By the methods described in the chapter 4-5, one reflecting surface profile is measured with a high accuracy. In shape measurement of a thin glass plate the rear surface profile cannot be measured by the method of the chapter 5 because the dispersion effect exists in the glass plate. The position Z_p of π phase nearest the position Z_a of amplitude maximum in the CVIS is not equal to the position of the rear surface. From simulation results it is made clear that the positions Z_a and Z_p are proportional to the rear surface position or the thickness of the glass plate. The proportional coefficients for Z_a and Z_p are determined to $C_a=1.53612$ and $C_p=1.51506$, respectively, by the simulations. Since the position interval of 2π phase change is $\lambda_A/2$ and the position Z_p is selected to be nearest to the position Z_a , the position Z_p changes suddenly by $\lambda_A/2$ when the distance between the position Z_p and the position Z_a becomes $\lambda_A/4$. λ_A is a weighted average wavelength in the spectral distribution of light source. The number n_j of occurrences of this position jump in the position Z_p can be calculated from C_a , and C_p values. By using an exact thickness measurement of the thin glass plate is made by using the Z_p value after eliminating the $(\lambda_A/2)n_j$ value. The measurement errors of front and rear surface profile are less than 4 nm. The measured thickness has an error less than 4 nm and the repeatability is 2.4 nm.

Chapter 7: The main sentence of dissertation is summarized.

CHAPTER 2

COMPLEX-VALUED INTERFERENCE SIGNAL IN WHITE-LIGHT SCANNING INTERFEROMETER

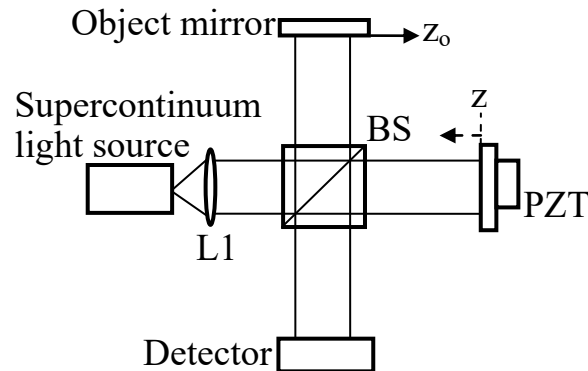


Fig. 2.1. Schematic of a white-light scanning interferometer.

2.1 Theory

2.1.1 Interference signal detected in white-light scanning interferometer

Figure 2.1 shows a Michelson interferometer that has a supercontinuum light source and a PZT. A light emitted from the laser source is expanded as the parallel beam by a Lens L1. The beam-splitter (BS) makes the beam transmit to two perpendicular directions. One of the beams goes to the object with the position of Z_o . The other beam goes to the reference mirror connected with the PZT. Position z changes with the movement of the PZT. The detector captures the interference signal generated by two reflected beams from object and reference mirror. When the PZT moves, the interferometer is a white-light scanning interferometer (WLSI). Since the refractive index of optical component is related to the wavelength, the OPDs are different for interference signals with different wavelengths. The non-linear OPD for different wavelengths in white-light interference signal is denoted as dispersion phase. The random noise also needs to be considered in the interference signal. The effect of dispersion phase and random noise are discussed in this chapter.

The white-light interference signal with and without dispersion phase are shown by the red and black in Fig. 2.2. The function of ideal interference signal is given by

$$S(z) = \int_{-\infty}^{\infty} I(\sigma) \cos[4\pi(z - Z_o)\sigma] d\sigma, \quad (2.1)$$

The function of actual interference signal is given by

$$S(z) = \int_{-\infty}^{\infty} I(\sigma) \cos[4\pi(z - Z_o + \varphi_n(z))\sigma + \varphi_d(\sigma)] d\sigma, \quad (2.2)$$

where σ is wavenumber, and $I(\sigma)$ is the spectral intensity of the light source. The $\varphi_d(\sigma)$ is a dispersion phase. The $\varphi_n(z)$ is the random noise.

2.1.2 Complex-valued interference signal

In order to obtain the complex-valued interference signal, the Fourier transform (FT) is performed on the ideal and actual interference signals. The amplitude and phase distribution are obtained in wavenumber domain. Fourier transform of ideal signal in the region of positive wavenumbers is derived as

$$FT[F(\sigma)] = I(\sigma)e^{-j4\pi Z_o\sigma}, \quad (\sigma > 0), \quad (2.3)$$

In wavenumber domain, the amplitude is smooth and the phase is the linear line for ideal interference signal. Because of the effect of dispersion phase, random noise, and not linear scanning of PZT, there are distortions on the amplitude and the phase is not linear for actual signal.

The inverse Fourier transform (IFT) is performed on amplitude and phase distribution in wavenumber domain to obtain the complex-valued interference signals (CVISs) are shown in the right parts of Fig. 2.2.

Expressing the inverse Fourier transform (IFT) of $I(\sigma)$ by $A(L)e^{j\alpha(L)}$, the CVIS of ideal interference signal is given by

$$S(z) = A(2z - 2Z_o) \exp[j\alpha(2z - 2Z_o)]. \quad (2.4)$$

The object position Z_o is obtained from the CVIS.

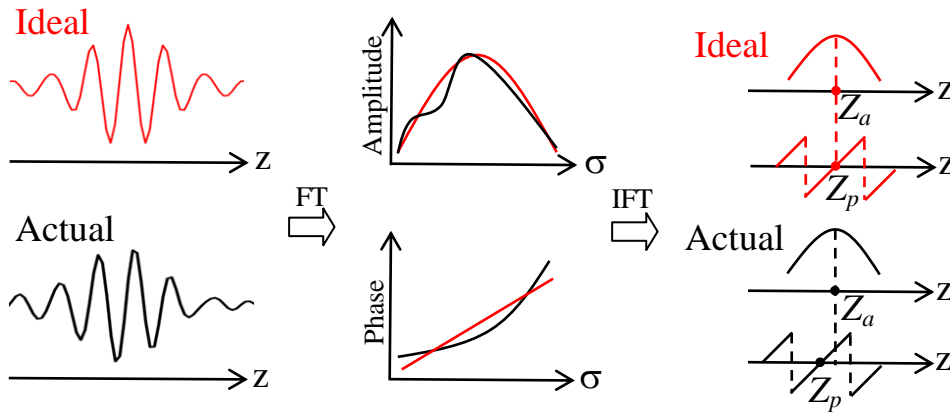


Fig. 2.2. Signal processing for ideal and actual interference signals.

2.1.3 Measurement values of Z_a and Z_p

The position of the maximum amplitude value is denoted as Z_a . The zero phase position nearest Z_a is denoted as Z_p . Since the experimental data is a discrete interference signal, the maximum value of the amplitude is not the exact peak value of amplitude distribution. The interpolation is carried out to add more sampling points of amplitude distribution and the exact Z_a value is obtained from the peak position of this interpolated amplitude distribution. The discrete phase distribution also cannot provide an exact zero phase position nearest Z_a . After selecting a few sampling points of phase nearest Z_p , the first-order equation of phase is calculated by least square method. The exact Z_p value is calculated by the first-order equation.

From the CVIS of ideal interference signal, the $Z_a=Z_p$ means that the ideal interference signal provides the exact object position. In the CVIS of actual interference signal, the $Z_a\neq Z_p$ means that it is hard to obtain the exact object position. In order to obtain the ideal interference signal, the effect of dispersion phase, random noise, and not linear scanning of PZT on the phase of actual interference signal in wavenumber domain should be eliminated.

2.2 Conclusion

The measurement value of Z_a and Z_p are proposed as the measurement value in this dissertation. When the three bad effects of dispersion phase, random noise, and not linear scanning of PZT exist, the $Z_a\neq Z_p$ indicates that it is hard to obtain the exact measurement value of Z_o . In order to approach to the ideal interference signal, the signal processing methods are proposed to eliminate these three bad effects from the actual interference signal. In chapter 3, the characteristics of Z_a and Z_p will be discussed. A method to eliminate the dispersion phase is proposed to improve the measurement accuracy.

CHAPTER 3

DISPERSION PHASE ELIMINATION BY USING SPECTRAL ANALYZER

3.1 Introduction

Complex-valued interference signals (CVISs) of a white-light scanning interferometer (WLSI) and a spectrally resolved interferometer (SRI) are obtained from their real-valued interference signals by the method described in chapter 2. In this chapter, it is made clear with a SRI that the magnitude of the dispersion phase caused by cubic beam-splitter changes linearly. Next a surface profile of an optical mirror is measured by WLSI. In wavenumber domain the dispersion phase detected by SRI is eliminated. The conventional measurement value is obtained from the slope of linear component of phase in wavenumber domain. A complex-valued interference signal is obtained through inverse Fourier transform of the dispersion-free spectral distribution in wavenumber domain, and the values of Z_a and Z_p are obtained. It is verified that the surface profile obtained from Z_p is more accurate than that from the slope of the linear phase component.

3.2 Principle

3.2.1 Dispersion phase of beam-splitter

Figure 3.1 shows the schematic of a white-light scanning interferometer. L2 and L3 are two achromatic lenses. Two optical fields on the object and reference surface are made with the two lenses of L2 and L3 with unity magnification on the detection plane. The detector is a high-speed camera. Figure 3.2 shows the structure of beam-splitter (BS). The two unequal sides of the BS generate the $\varphi_d(\sigma)$. The two beams reflected from the object surface and the reference surface have path distances of l_1 and l_2 in the BS, respectively. Denoting the distance difference by $l_\varepsilon=l_1-l_2$, one of beams divided by BS passes the extra part l_ε . The other beam goes across the same length of l_ε in the air whose refractive index is denoted as 1. The formula of dispersion phase is given by

$$\varphi_d(\sigma) = 4\pi[n(\sigma) - 1]\sigma l_\varepsilon, \quad (3.1)$$

where $n(\sigma)$ is the refractive index of the beam splitter. In the research, most of optical components are made of N-BK7 whose refractive index distribution is shown in Fig. 3.3. l_ε is a linear function of the position x where the two beams go out from the beam splitter. At $x=x_B$ the value of l_ε is almost equal to zero and it increases linearly as the position x approaches x_A . Defining $l_\varepsilon = \gamma d_\varepsilon$ where d_ε is value of l_ε at x_A position and γ is a value from 0 to 1 corresponding the x direction, the dispersion phase output along x direction of BS is given by

$$\varphi_d(\sigma) = 4\pi[n(\sigma) - 1]\gamma d_\varepsilon \sigma, \quad (3.2)$$

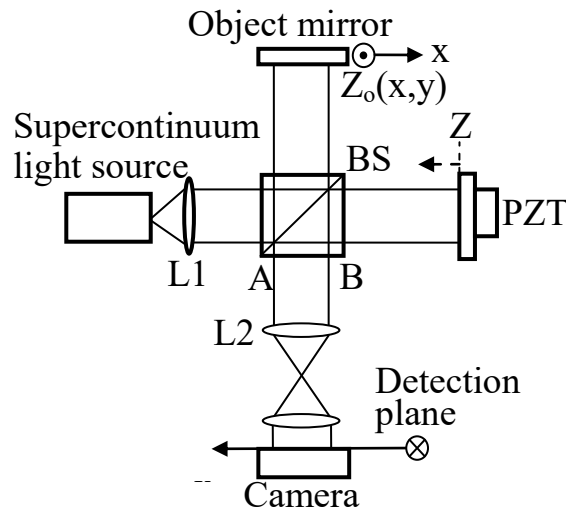


Fig. 3.1. Schematic of a white-light scanning interferometer.

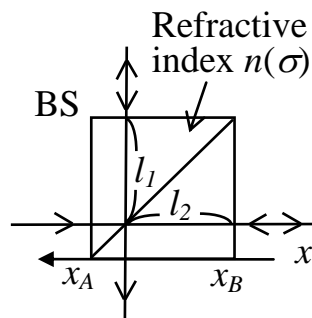


Fig. 3.2. Generation of dispersion phase by distance difference of $l_\varepsilon = l_1 - l_2$ in the beam splitter.

In order to confirm the dispersion mode described as Eq. (3.2), the dispersion phase of interference signal was detected on positions of detection plane as shown in Fig. 3.4. The interval of the detection points was

4 mm. The x -axis corresponds to the line A-B whose length was 25 mm. Detection point b was about on the center of the x -y surface of the beam splitter.

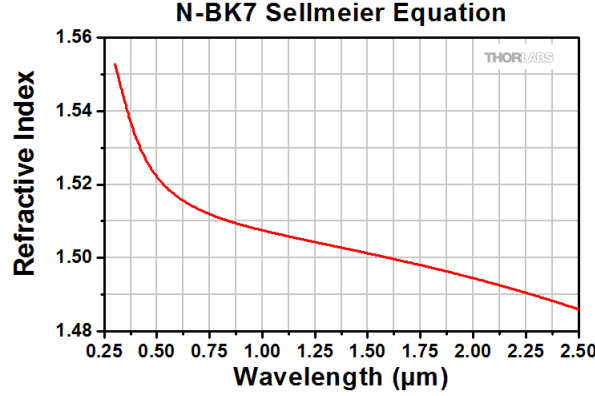


Fig. 3.3. The refractive index of material of N-BK7. (Provided by Thorlab)

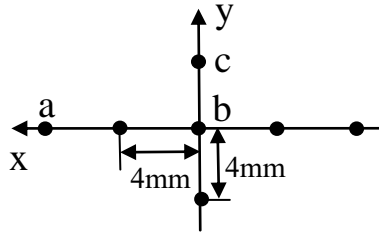


Fig. 3.4. Measurement points in the SRI on the detection plane.

3.2.2 Spectral resolved interferometer

Figure 3.1 shows the spectrally resolved interferometer (SRI) when the detector is spectral analyzer and the reference surface is stable. The SRI is used to detect the dispersion phase. The spectral interference signal expressed as a function of $L=2z-2z_o$ is given by

$$S_s(\sigma) = I(\sigma) \cos[2\pi L\sigma + \varphi_d(\sigma)], \quad (3.3)$$

3.2.3 Elimination of dispersion phase

A measured dispersion phase is denoted by $\varphi_{d,b}(\sigma)$ after a linear and bias components are eliminated from a dispersion phase $\varphi_d(\sigma)$ detected at one position at the b point in Fig. 3.4. The dispersion phase $\varphi_d(\sigma)$ without a linear and bias components is denoted by $\varphi_x(\sigma)$ along x direction. It is assumed that the sum of the absolute differences of $|\varphi_x(\sigma) - w_x \varphi_{d,b}(\sigma)|$ over the wavenumber σ has a minimum value when the value of w_x is equal to $W(x)$ as a function of x . In experiments $W(x)$ is not completely a linear function of x , and a value of $W(x)$ increases nearly in proportional to x . If the

linear component of $W(x)$ is expressed by $ex+e_0$, the dispersion phase which should be subtracted from $\varphi_d(\sigma)$ detected at a point of x is given by

$$\varphi_{d,x}(\sigma) = (ex + e_0) \varphi_{d,b}(\sigma) . \quad (3.4)$$

3.3 Experiment

3.3.1 Detection of dispersion phase

In experiment, both the object and reference surfaces were uncoated optical mirrors with flatness of one-eighth wavelength. The mirrors were regarded as one reflecting surface. The two optical fields existing on the object and reference surfaces, respectively, were made with the two lens of L2 and L3 with unity magnification on the detection plane. The light source of the interferometer was a supercontinuum light source whose spectral range was 500nm-1400nm. A spectral analyzer was used to detect the dispersion phase on the detection plane by the SRI. The interference signal detected at point b as shown is shown in Fig. 3.5. The wavenumber range of the interference signal was 1.1-2.1 μm^{-1} and the data number of the interference signal was 1024. Fourier transform was performed on the $S_S(\sigma)$ to obtain the amplitude and phase distribution. Figure 3.6 shows the amplitude and phase distribution in the region z of 17.5-27.5 μm . A rectangular window was multiplied by the Fourier transform of the interference signal to select the positive part. Inverse Fourier transform was performed on this windowed data to get the complex-valued interference signal (CVIS) as shown in Fig. 3.7. Since the amplitude distribution of the CVIS was almost zero outside the wavenumber region of 1.15-2.0 μm^{-1} , a linear component and a bias component were eliminated from the phase distribution of the CVIS in the region of 1.15-2.0 μm^{-1} to get the dispersion phase shown in Fig. 3.7(b).

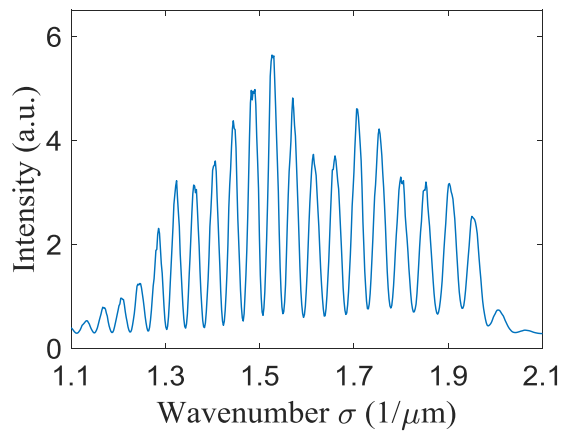
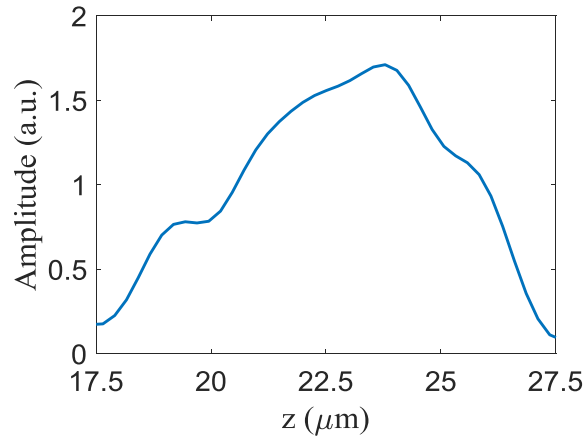
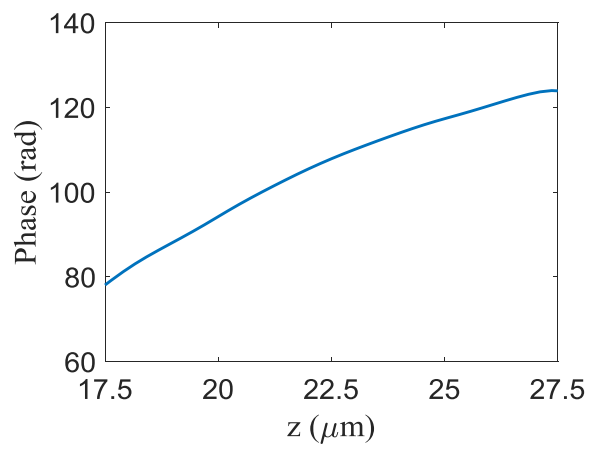


Figure 3.5 shows an interference signal detected by SRI at point b.

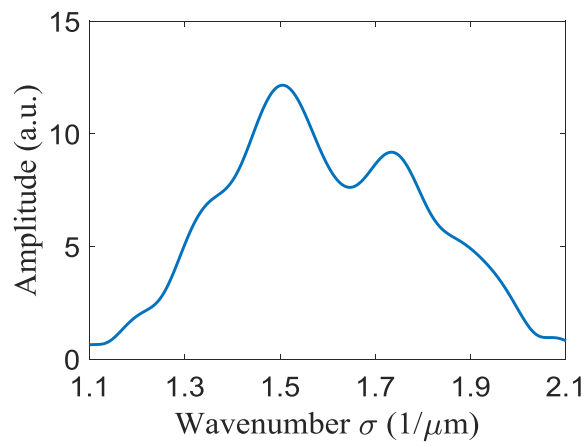


(a)

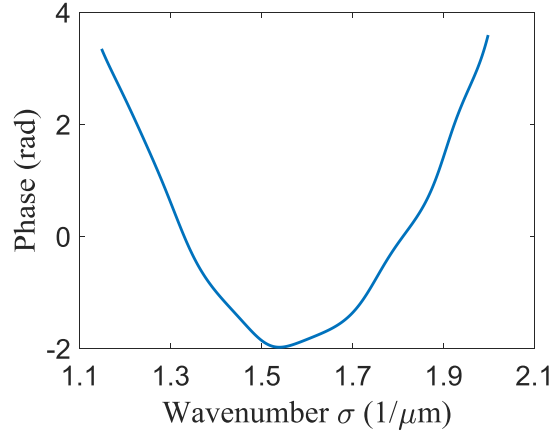


(b)

Fig. 3.6. Fourier transform of interference signal of Fig. 3.5. (a) amplitude and (b) phase.



(a)



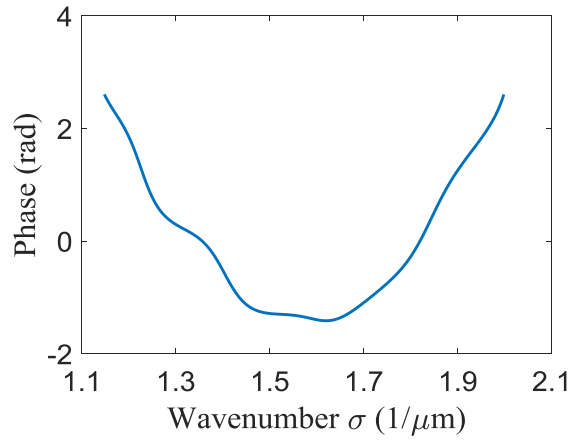
(b)

Fig. 3.7. Complex-valued interference signal of Fig. 3.5. (a) amplitude (b) phase without linear component.

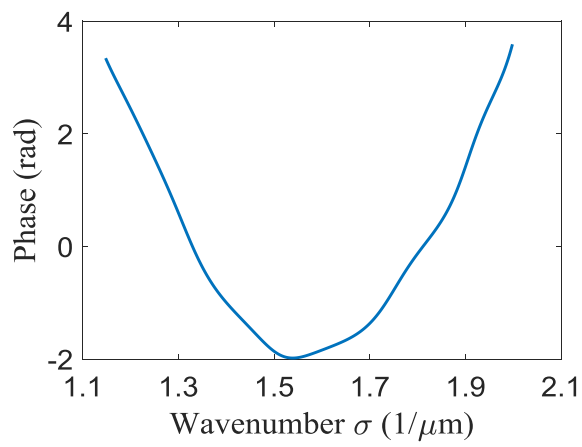
When the detection point was moved to the two points along the y -axis, the detected dispersion phases were almost same as that detected at point b. Figure 3.8(c) shows the dispersion phase detected at point c. Finally, when the detection point was moved to the five points along the x -axis, the magnitude of the detected dispersion phases was nearly proportional to the coordinate value of the x -axis while its waveform almost did not change. Figure 3.8(a) shows the dispersion phase detected at point a.

It has been made clear that the magnitude of the dispersion phase changes along the x axis and does not change along the y axis. In order to eliminate the dispersion phase in surface profile measurements, a distribution of the dispersion phase along the x axis was made by using the dispersion phase detected at point b as $\varphi_{d,b}(\sigma)$ that was defined in Sec. 3.2.3. The measurement point on the camera along x axis was expressed by $x=N_x\Delta x$ in Eq. (3.4), where N_x was number of the measurement points and Δx was its interval. Since the values of e and e_0 were $-0.0083/\Delta x$ and 1.25, respectively, Eq. (3.4) was rewritten as

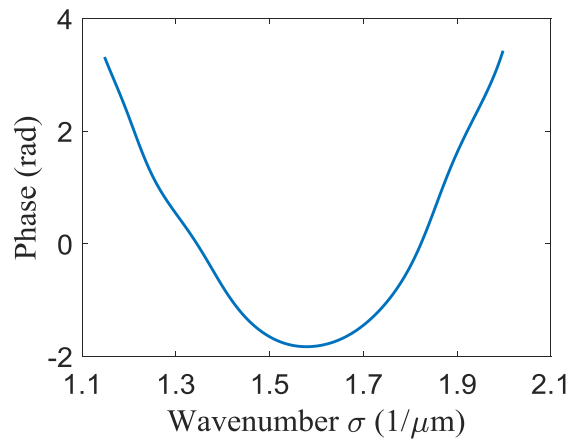
$$\varphi_{d,x}(\sigma) = (1.25 - 0.0083N_x)\varphi_{d,b}(\sigma). \quad (3.5)$$



(a)



(b)



(c)

Fig. 3.8. Dispersion phase distributions detected at different detection points; (a) point a, (b) point b, and (c) point c.

3.3.2 Signal acquisition and processing

A high-speed camera was used as the detector and its pixel size was $20\ \mu\text{m} \times 20\ \mu\text{m}$. The frame size was 640×480 pixels. An interference signals detected on one pixel was used in the regions of 10×10 pixels, and the

measurement points of 56×41 pixels with the interval of $200 \mu\text{m}$ was made for the surface profile measurement. The measuring points were denoted by N_x and N_y . N_x was from 1 to 56, and N_y was from 1 to 41. The reference surface was moved by the PZT at a constant velocity of about $80 \mu\text{m/s}$, and the sampling interval Δz of the interference signal was 39.6 nm in the scanning white-light interferometer. The data number N of the detected interference signal was 1024, and a required interference signal was selected with a rectangular window whose data number was 240. The other data outside the window were zero values. Figure 3.9 shows the windowed interference signal detected at a measurement point of $N_x=30$ and $N_y=18$ nearly equal to point b in Fig. 3.4. Fourier transform was performed on this windowed interference signal of data number $N=1024$. The variable in the Fourier transform of the interference signal was wavenumber σ and its interval was $\Delta\sigma=1/(2N\Delta z)=0.0123\mu\text{m}^{-1}$. Figures 3.10(a) and (b) show amplitude and phase of the Fourier transform of the interference signal, respectively. Amplitude was almost zero outside the wavenumber range of $1.15\text{-}2.0 \mu\text{m}^{-1}$. The blue line in Fig. 3.10(b) was the measured phase distribution. The dispersion phase given by Eq. (3.5) was subtracted from the blue line to get the dispersion-free phase shown by the red line. Since the dispersion-free phase is nearly equal to a linear line, a least square fitted line was calculated as shown by the dot line. By performing inverse Fourier transform on the complex-valued data of the amplitude and the dispersion-free phase of Fig. 3.10, the complex-valued interference signal was obtained as shown in Fig. 3.11. The position of maximum amplitude was denoted by Z_a , and the position Z_p of zero phase nearest to Z_a was another measurement value obtained from the phase distribution in the CVIS. In Fig. 3.11 the position Z_a of $-1.898 \mu\text{m}$ determined the measured position Z_p of $-1.940 \mu\text{m}$.

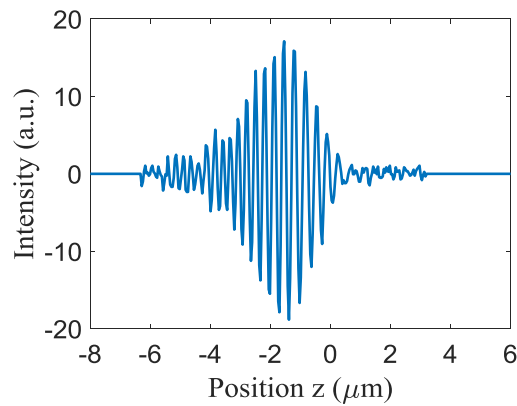
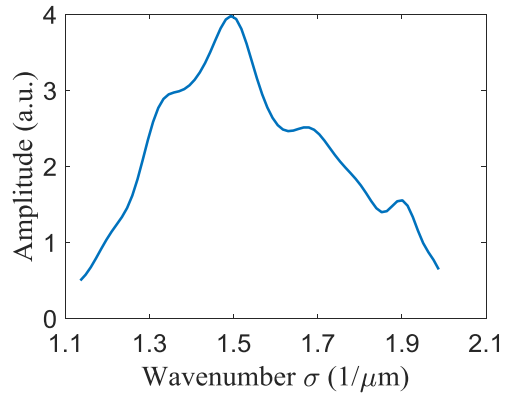
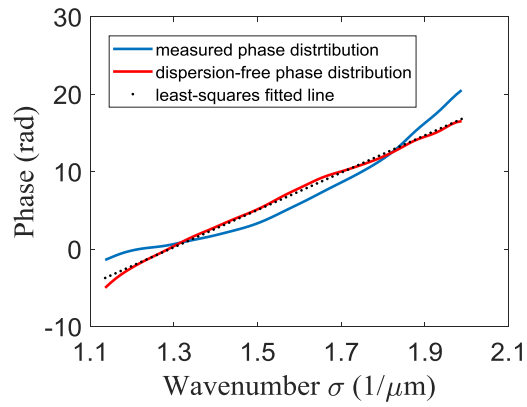


Fig. 3.9. Interference signal detected at a measurement point of $N_x=30$ and $N_y=18$ on the camera.

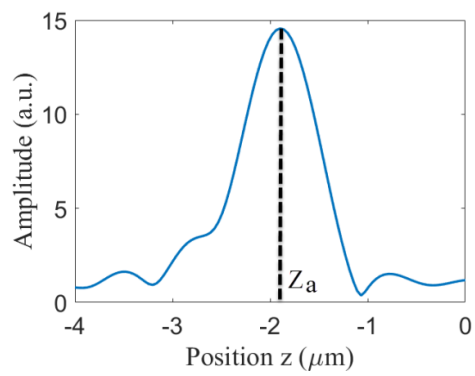


(a)

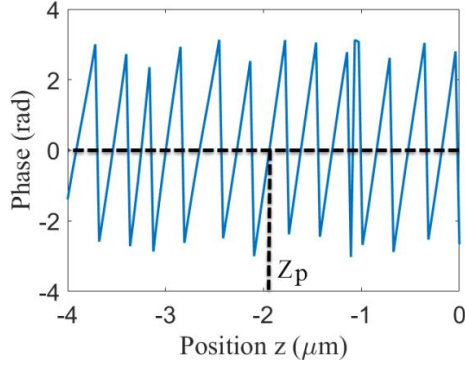


(b)

Fig. 3.10. Fourier transform of the interference signal of Fig. 3.9. (a) amplitude and (b) phase.



(a)



(b)

Fig. 3.11. Complex-valued interference signal of Fig. 3.9 at $N_x=30$ and $N_y=18$ after eliminating the dispersion phase. $Z_a=-1.898\mu\text{m}$ and $Z_p=-1.940\mu\text{m}$. (a) amplitude and (b) phase.

3.4 Measurement result

The signal processing to obtain the two measurement values of Z_s and Z_p was carried out for all of the measurement points to get surface profiles of the optical mirror. The dispersion phase to be subtracted from the spectral phase detected at a measurement point of N_x was given by Eq. (3.5). A surface profile obtained from the measured values of Z_s is shown in Fig. 3.12, where the tilt and piston components were eliminated. Small variations with the magnitude less than 12 nm exist, and spike-like large variations appear in the upper-left corner due to small amplitudes of the interference signals. In order to confirm clearly these small variations, Fig. 3.13 shows one-dimensional distribution along N_x at $N_y=20$ in the surface profile of Fig. 3.12. A surface profile obtained from measured values of Z_p is shown in Fig. 3.14, where the tilt and piston components were eliminated. There are many step-like variations whose width was about $0.320\mu\text{m}$. The value of $0.640\mu\text{m}$ was nearly equal to the weighted average wavelength λ_A $0.638\mu\text{m}$. This step-like jump is denoted as $\lambda_A/2$ position jump. The three regions indicated with A, B, and C in Fig. 3.14 are distinguished by the two boundaries where the step change in Z_o value occurred. In Fig. 3.11 one period in the wrapped phase distribution was also about $0.320\mu\text{m}$ around the position of Z_a .

In order to make a continuous surface profile, for the measurement points in the region B a value of $-0.320\mu\text{m}$ was added to the measured value of Z_p . Similarly in the region C a value of $-0.320\mu\text{m}$ was subtracted from the measured value of Z_p to obtain an exact position. This correction is called $\lambda_A/2$ position jump correction. A surface profile after the $\lambda_A/2$ position jump correction is shown in Fig. 3.15, where the tilt and piston components were eliminated again. The measured surface profile was very smooth, and the

magnitude of the small variations was less than 4 nm. In order to confirm clearly the small variations, Fig. 3.16 shows one-dimensional distribution along N_x at $N_y=20$ in the surface profile of Fig. 3.15. The repeatability was obtained by calculating a root-mean-square value of the difference between two surface profiles measured in an interval of a few ten minutes. The repeatability was 1.2 nm in the measurement by Z_p , while it was 13.2 nm in the measurement by Z_s . It was made clear that the measurement value Z_p provides more exact position of a reflecting surface than the measurement value Z_s .

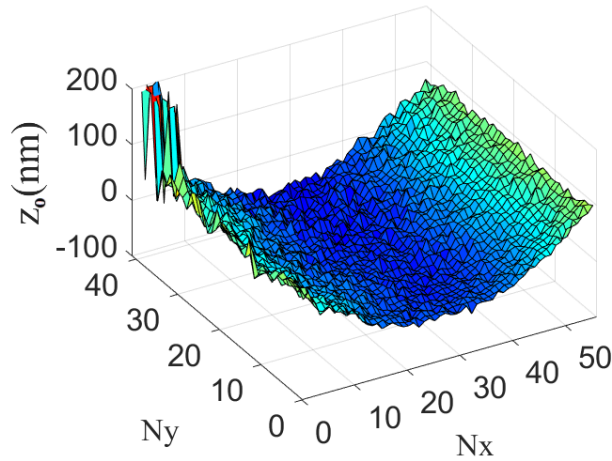


Fig. 3.12. Surface profile obtained from the measured values of Z_s .

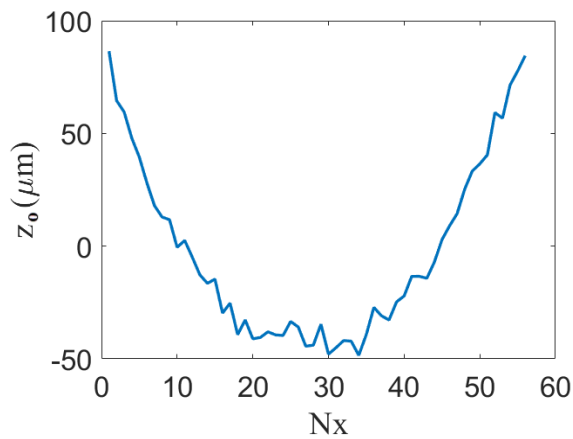


Fig. 3.13. One-dimensional distribution along N_x at $N_y=20$ in the surface profile of Fig. 3.12.

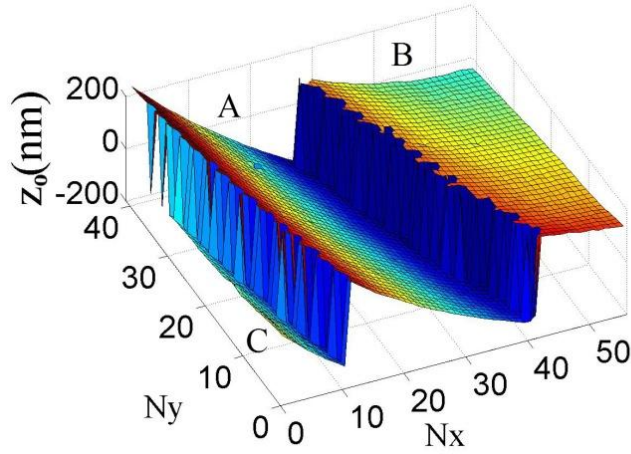


Fig. 3.14. Surface profile obtained from the measured values of Z_p by using Eq. (3.5).

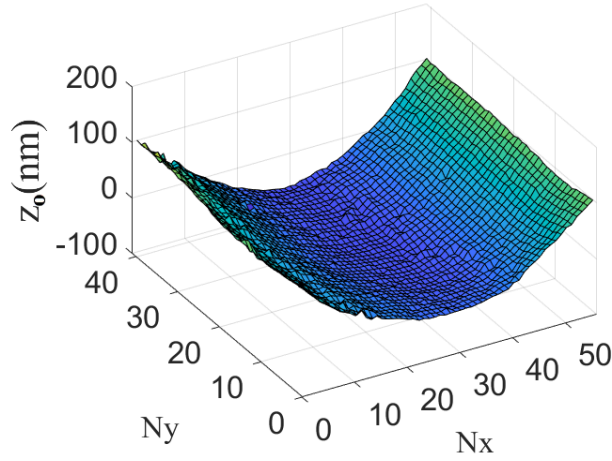


Fig. 3.15. Surface profile obtained from Fig. 3.14 after the $\lambda_A/2$ position jump correction.

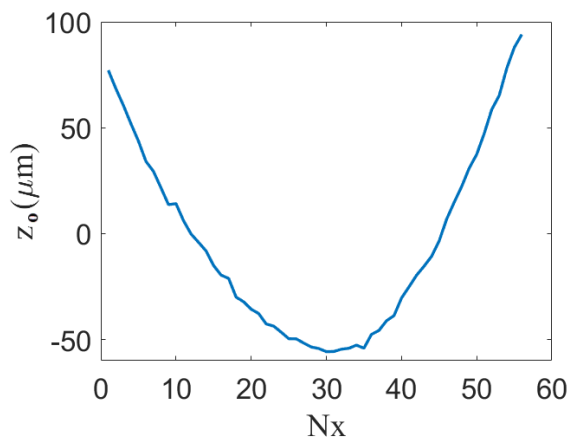


Fig. 3.16. One-dimensional distribution along N_x at $N_y=20$ in the surface profile of Fig. 3.15.

In order to make sure of the requirement of eliminating the dispersion phase, a surface profile was obtained without eliminating the dispersion phase. This surface profile after the $\lambda_A/2$ position jump correction is shown in Fig. 3.17. Although the $\lambda_A/2$ position jump correction was performed, there were still spike-like variations with height more than $0.320\ \mu\text{m}$. And also there was a step-like variation with width more than $0.320\ \text{nm}$ in the upper-right corner of the region B. It was confirmed that the elimination of the dispersion phase is required to get an exact surface profile.

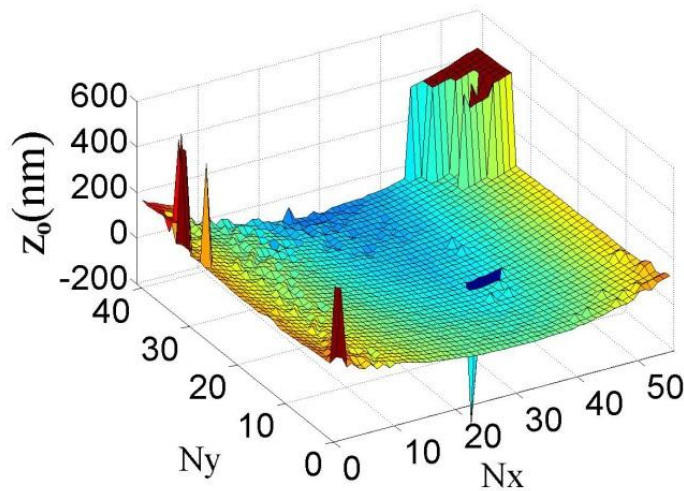


Fig. 3.17. Surface profile obtained from the measured values of Z_p without eliminating the dispersion phase after the $\lambda_A/2$ position jump correction.

3.5 Conclusion

The CVISs of the WLSI and the SRI were obtained from the real-valued interference signals through Fourier transform. First the phase distribution in the CVIS of the SRI indicated the dispersion phase caused by the two sides of unequal length in the beam-splitter, and it was shown by the experiments that the magnitude of the dispersion phase changed linearly along the horizontal direction of the beam-splitter. Next the surface profile measurements were made with the WLSI. The dispersion phase with a different magnitude was subtracted from the spectral phase in Fourier transform of the real interference signal of the WLSI. The dispersion-free CVIS was obtained through inverse Fourier transform of this spectral distribution, and the position Z_p of zero phase nearest to the position Z_a of amplitude maximum provided an accurate surface profile with an error less than $4\ \text{nm}$ after the $\lambda_A/2$ position jump correction, while the surface profile obtained by the position Z_s calculated by the linear component of the spectral phase contained errors less than $12\ \text{nm}$. It was made clear that the

utilization of the CVIS of the WLSI and SRI could achieve highly accurate measurements of surface profile.

CHAPTER 4

DISPERSION PHASE ELIMINATION BY USING A LEAST SQUARE LINE IN SPECTRAL PHASE DISTRIBUTION

4.1 Introduction

The chapter 3 describes a method to detect the dispersion phase of different position on the detection plane by using SRI. The detected dispersion phase is subtracted from the white-light interference signal in wavenumber domain. In order to simplify the experiment, a new signal processing to eliminate the dispersion phase without detection of dispersion is proposed. The linear and bias components in the spectral phase distribution are used to calculate the complex-valued interference signal. The chapter 3 shows the magnitude of the dispersion phase changed linearly along the horizontal direction of the beam-splitter. Thus a simulation is carried out to verify that the dispersion phase generates an inclination in the measured surface profile along horizontal direction. The simulations also show the random phase noise changes the slope of the linear component, but the position of zero phase nearest to the position of amplitude maximum in the CVSI almost does not change due to the bias component. These characteristics guarantee the high accurate measurement by the new signal processing without using the dispersion phase measured with a spectrally resolved interferometer.

4.2 Principle

4.2.1 Least square line in spectral phase distribution

Figure 4.1 shows a WLSI same with Fig. 3.1. An interference signal is detected with a camera when the PZT is moving. The interference signal expressed as a function of the scanning position z is given by

$$S(z) = \int_{-\infty}^{\infty} I(\sigma) \cos[4\pi(z - Z_o)\sigma + \varphi_n(z)\sigma + \varphi_d(\sigma)] d\sigma, \quad (4.1)$$

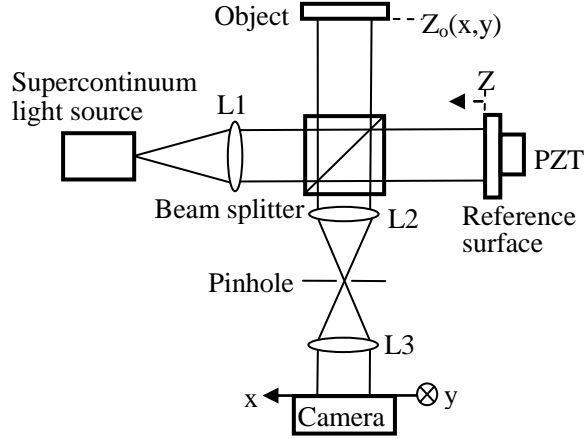


Fig. 4.1. Schematic of a white-light scanning interferometer.

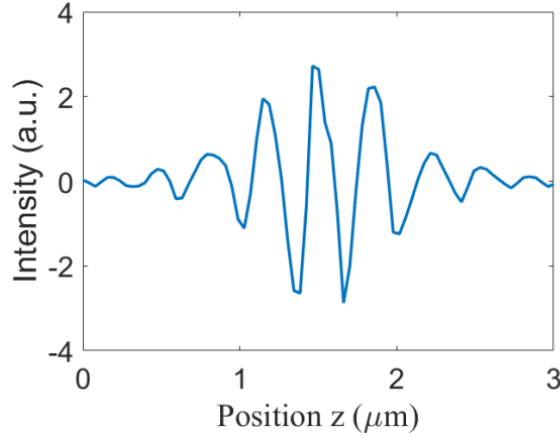


Fig. 4.2. Interference signal $S(z)$ generated by Eq. (4.1).

where phase $\varphi_d(\sigma)$ is a dispersion phase caused by two sides of unequal length in a cubic beam splitter. Phase $\varphi_n(z)$ is generated by an optical path change which is caused by random disturbances such as mechanical vibrations and non-constant speed of the PZT movement. Figure 4.2 shows the interference signal generated by Eq. (4.1). Fourier transform of Fig. 4.2 is shown by Fig. 4.3. Fourier transform of $S(z)$ or the spectral distribution in the region of positive wavenumbers is expressed as

$$F(\sigma) = I_F(\sigma) e^{-j4\pi Z_0 \sigma} e^{j\beta(\sigma)}, \quad (\sigma > 0) \quad (4.2)$$

where $\beta(\sigma)$ is arisen from the phases $\varphi_n(z)\sigma$ and $\varphi_d(\sigma)$ through Fourier transform. Denoting the least squares line in the phase distribution of Eq. (4.2) by $a_0 + (a_1 - 4\pi Z_0)\sigma$, a new spectral distribution having only bias and linear phases is obtained as

$$F_L(\sigma) = I_F(\sigma)e^{j(a_1-4\pi Z_0)\sigma} e^{ja_0}, \quad (\sigma > 0) \quad (4.3)$$

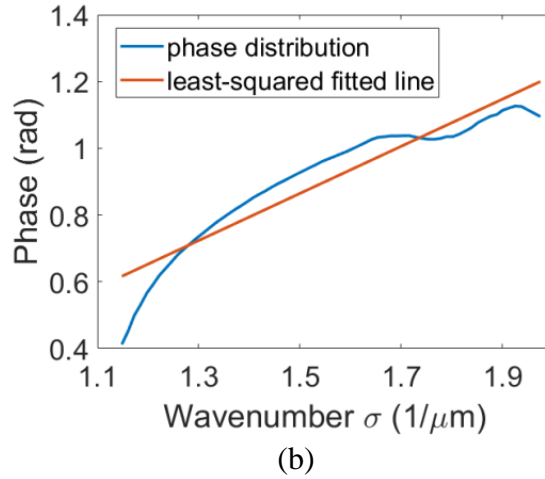
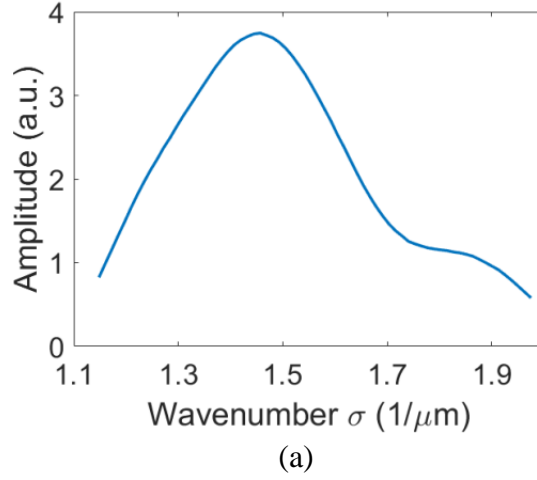


Fig. 4.3. Fourier transform of interference signal of Fig. 4.2. (a) amplitude and (b) phase.

Fourier transform of Fig. 4.2 is shown by Fig. 4.3. The blue line in Fig. 4.3(b) is the phase distribution $\beta(\sigma)-4\pi Z_0\sigma$ in the Eq. (4.2). There are nonlinear components in the phase distribution. The least squares line of the phase calculated by least square method is shown by the red line is $a_0+(a_1-4\pi Z_0)\sigma$. The values of a_0 and a_1 are affected by the dispersion phase or random noise. When there is no dispersion phase and random noise, the a_0 and a_1 are $2n\pi$ and 0, where n is an integer determined by the first unwrapping point of phase.

Expressing the inverse Fourier transform of $I_F(\sigma)$ by $A(2z)e^{j\alpha(2z)}$, the complex-valued interference signal (CVIS) derived as inverse Fourier transform of $F_L(\sigma)$ is given by

$$S(z) = A(z - Z_s) \exp[j\alpha(z - Z_s) + ja_0]. \quad (4.4)$$

where $Z_s=Z_0-(a_1/4\pi)$, $A(z)=A(-z)$, $\alpha(z)=-\alpha(z)$, and $\alpha(0)=0$. The period of the phase distribution in the CVIS is $\lambda_A/2$ around $z=Z_s$, where λ_A is the weighted average wavelength in the distribution of $I_F(\sigma)$.

4.2.2 Relation between Z_a and Z_p

Since the phase of complex-valued interference signal is wrapped, the value of a_0 in Eq. (4.4) exists in the range from $-\pi$ to π after the value of a_0 in Eq. (4.3) is reduced to $a_0-2\pi n$, where n is an integer. Equation (4.4) leads to the following results: a position Z_a of maximum amplitude of $A(z-z_s)$ is equal to the measurement value Z_s obtained from the slope of the linear component in the spectral phase. The position Z_p of zero phase nearest to the position Z_a is given by

$$Z_p = Z_s - (a_0 \lambda_A / 4\pi) = Z_0 - (a_1 / 4\pi) - (a_0 \lambda_A / 4\pi). \quad (4.5)$$

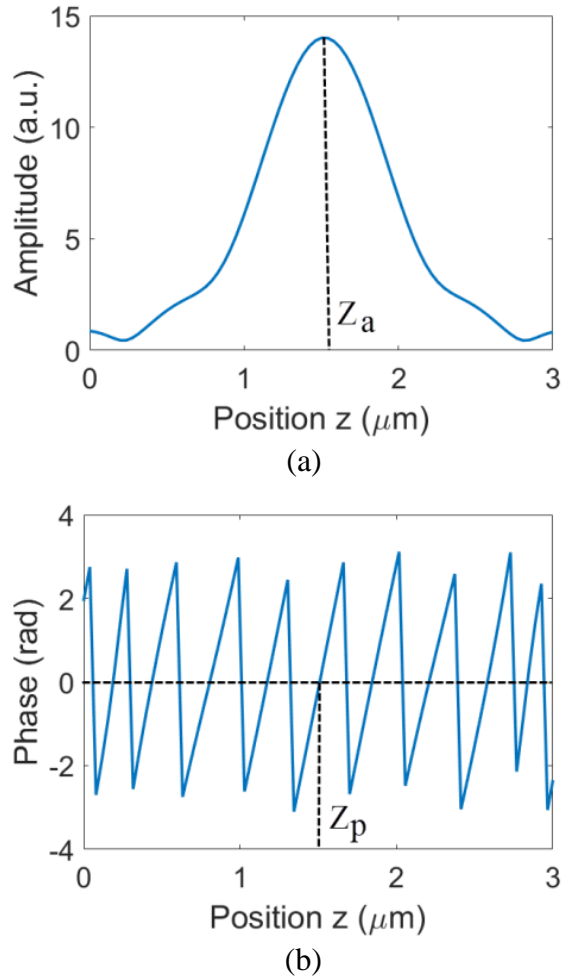


Fig. 4.4. Complex-value of the interference signal of Fig. 4.2. (a) amplitude and (b) phase.

4.3 Simulation

In order to generate the interference signal given by Eq. (4.1), the spectrum $I(\sigma)$, the phase distributions $\varphi_d(\sigma)$, and the random phase noise $\varphi_n(z)$ are necessary. Figure 4.5 shows the spectrum of the supercontinuum light source which was detected by a spectral analyzer. The wavenumber region of the detected spectrum was from 1.1 to 2.1 μm^{-1} . The difference between the lengths of the two sides of the beam splitter was about 100 μm . The non-linear component contained in the dispersion phase $\varphi_d(\sigma)$ at $l_\varepsilon=1 \mu\text{m}$ was calculated with least squared method as shown in Fig. 4.6. The dispersion phase $\varphi_d(\sigma)$ of $l_\varepsilon=40 \mu\text{m}$ around the central position of the beam splitter was used. Figure 4.7 is the random Gaussian noise $\varphi_n(z)$ with average of zero and variance of 0.09 $\text{rad}\cdot\mu\text{m}$. The interference signal was generated in the region from -30 μm to 30 μm where the object position Z_o was 1 μm , and the sampling interval Δz and the sampling number N were 0.0073 μm and 8192, respectively. A part of interference signal whose envelop value was more than one-tenth of its maximum intensity was selected by rectangular window whose width was from -23 μm to -18 μm , as shown in Fig. 4.8. The other data outside the rectangular window were zero values. Fourier transform was performed on this interference signal of data number N . The interval of wavenumber was $\Delta\sigma=1/(2N\Delta z)=0.0083 \mu\text{m}^{-1}$. Figures 4.9(a) show the amplitude $I_F(\sigma)$ of Fourier transform $F(\sigma)$. The values of a_0 and $a_1-4\pi Z_o$ were the -280.721 rad and 257.486 $\text{rad}\cdot\mu\text{m}$, respectively. The phase distribution of $F(\sigma)$ contained a large value of a_1 of 270.053 $\text{rad}\cdot\mu\text{m}$ which was almost caused by the dispersion phase at $l_\varepsilon=40 \mu\text{m}$. In order to show clearly the non-linear component contained in the phase of $F(\sigma)$, the phase distribution of $\beta(\sigma)-(a_1-4\pi z_o)\sigma$ is shown in Fig. 4.9(b), where the a_0 was equal to -280.721 $\text{rad}\cdot\mu\text{m}$. The measurement value z_s of the object position was obtained from the linear component of the phase distribution as $Z_s=Z_o-a_1/4\pi=-20.490 \mu\text{m}$. By performing inverse Fourier transform on the data of $F_L(\sigma)$, the CVIS was obtained as shown in Figs. 4.10(a) and (b). The values of Z_a was -20.490 μm which was equal to Z_s . The measurement value Z_p of the object position obtained from this CVIS was -20.596 μm .

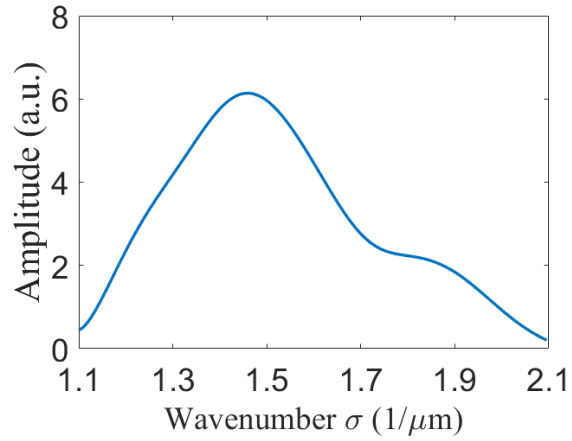


Fig. 4.5. Spectrum $I(\sigma)$ of the light source.

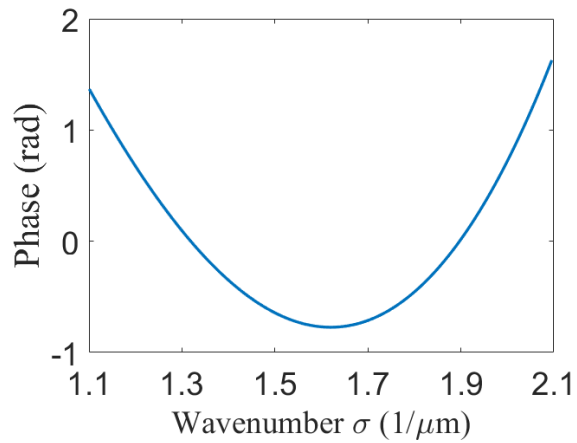


Fig. 4.6. Non-linear component contained in $4\pi[n(\sigma)-1]\sigma$.

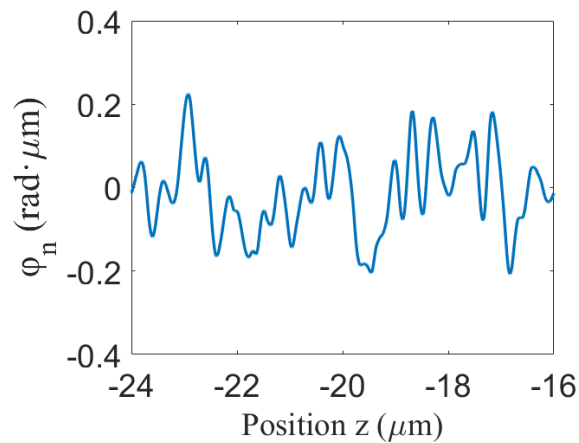


Fig. 4.7. Gaussian noise with average of zero and variance of $0.09 \text{ rad } \mu\text{m}$.

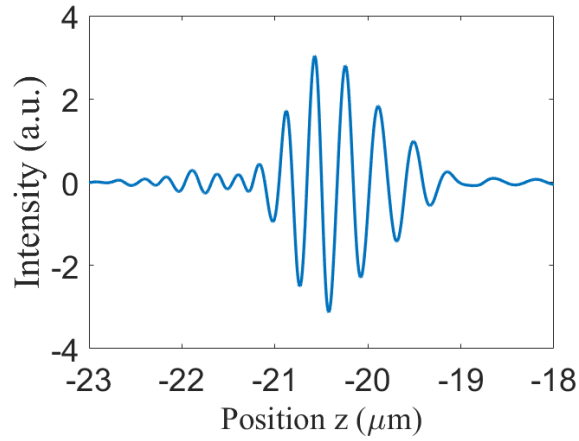
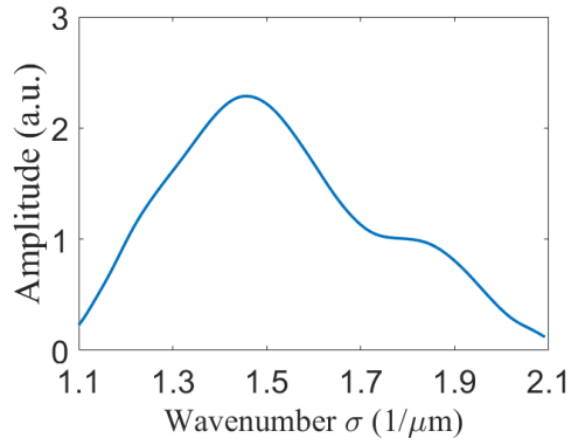
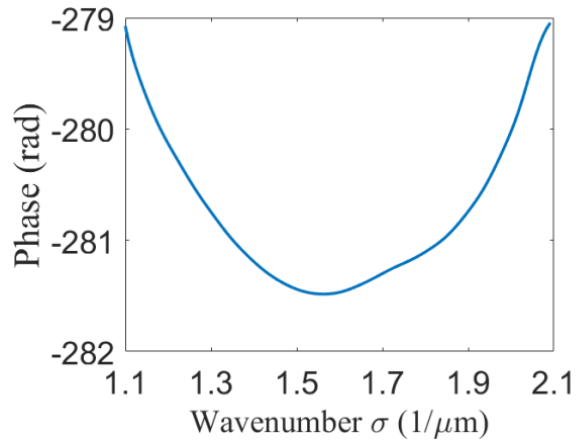


Fig. 4.8. Interference signal generated with the spectrum, the dispersion phase, and the Gaussian noise.



(a)



(b)

Fig. 4.9. Fourier transform of the interference signal of Fig. 4.8; (a) amplitude $I_F(\sigma)$ and (b) phase of $\beta(\sigma) - (a_1 - 4\pi Z_0)\sigma$.

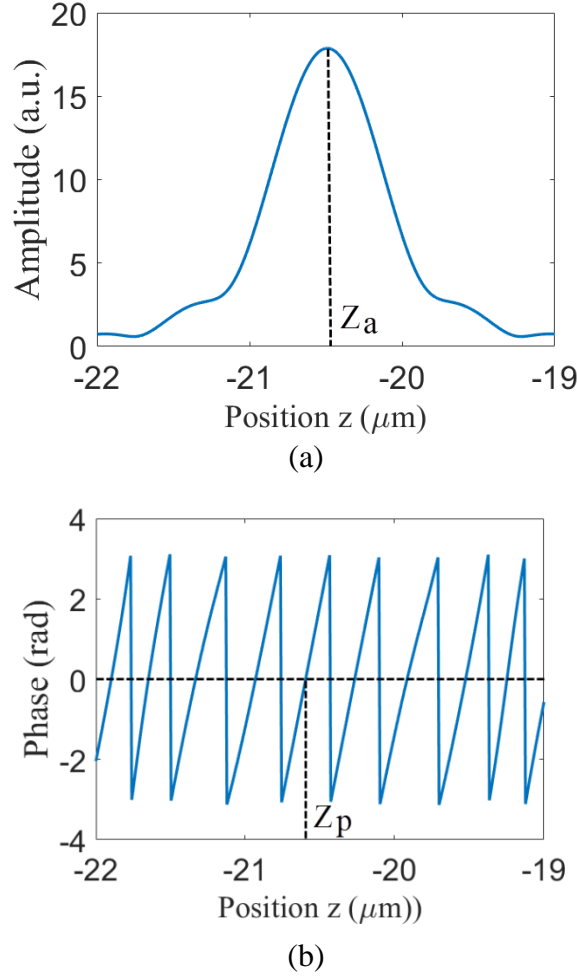


Fig. 4.10. Complex-valued interference signal of Fig. 4.8.

4.3.1 Effect of dispersion phase on measurement accuracy

In order to examine the effect of dispersion phase, the different values of l_ε were used in the simulation when the noise φ_n did not exist. Results are shown in Table 4.1. The values of a_0 and a_1 change linearly with the increase of l_ε . The interval in a_0 and a_1 between of the adjacent values of l_ε were constant by ignoring small fluctuations less than 5 nm and 3 rad· μm , respectively. The average value of the interval in a_0 and a_1 were about 73.470 rad and 67.604 rad· μm , respectively. The values Z_s-Z_o and Z_p-Z_o were obtained from the CVIS. These two values almost satisfied Eq. (4.5). The decreasing interval in the values of Z_s-Z_o between adjacent values of l_ε was a constant value of 5.380 μm by ignoring fluctuations less than 1 nm. On the other hand, the interval of 5.152 μm in the values of Z_p-Z_o between $l_\varepsilon=10 \mu\text{m}$ and $l_\varepsilon=20 \mu\text{m}$ is not equal to the constant interval of 5.481 μm between the other adjacent values of l_ε . After adding a value of $\lambda_A/2=0.329 \mu\text{m}$ to the values of Z_p-Z_o at $l_\varepsilon=20 \mu\text{m}$, 30 μm , and 40 μm , all the intervals in Z_p-Z_o between the adjacent values became the constant value of 5.481 μm . It is made clear from the results in Table 4.1 that the dispersion phase brings

only an inclination along the x axis to a measured surface profile. Therefore the dispersion phase has no influence on the measurement accuracy.

Table 4.1. Simulation results at the different values of l_ε without noise.

l_ε (μm)	0	10	20	30	40
a_0 (rad)	12.566	-60.903	-134.371	-207.841	-281.312
a_1 (rad μm)	0.0	67.604	135.206	202.811	270.415
Z_s-Z_o (μm)	0.0	-5.380	-10.759	-16.139	-21.519
Z_p-Z_o (μm)	0.0	-5.481	-10.633	-16.113	-21.594

The simulation was carried out when the dispersion and noise existed together. The simulation results are shown at Table 4.2. Although all the values are different from the results in Table 4.1, the values of Z_s-Z_o and Z_p-Z_o also satisfy Eq. (4.5). Due to the effect of noise, the interval in the values of Z_s-Z_o between the adjacent values of l_ε was not constant, and the deviations from the average value of $5.369 \mu\text{m}$ were less than 60 nm . The interval of $5.151 \mu\text{m}$ in the values of Z_p-Z_o between $l_\varepsilon=10 \mu\text{m}$ and $l_\varepsilon=20 \mu\text{m}$ was not equal to the constant interval of $5.482 \mu\text{m}$ between the other adjacent values of l_ε . After adding a value of $\lambda_A/2=0.329 \mu\text{m}$ to the values of Z_p-Z_o at $l_\varepsilon=20 \mu\text{m}$, $30 \mu\text{m}$, and $40 \mu\text{m}$, all the intervals in Z_p-Z_o became almost constant, and the deviations from the average value of $5.482 \mu\text{m}$ was less than 4 nm . Therefore the noise has a large influence on the linear change in the values of Z_s-Z_o , compared with the values of Z_p-Z_o .

Table 4.2. Simulation results at the different values of l_ε with noise.

l_ε (μm)	0	10	20	30	40
a_0 (rad)	12.242	-60.381	-134.747	-208.636	-280.721
a_1 (rad μm)	0.185	67.237	135.419	203.301	270.052
Z_s-Z_o (μm)	-0.015	-5.351	-10.776	-16.178	-21.490
Z_p-Z_o (μm)	0.002	-5.479	-10.630	-16.110	-21.596

4.3.2 Effect of random noise on measurement accuracy

In order to show degree of noise resistant, the values of Z_s-Z_o and Z_p-Z_o were compared between the Table 4.1 and Table 4.2. The differences of the values are denoted by $\Delta(Z_s-Z_o)$ and $\Delta(Z_p-Z_o)$ in Table 4.3. The $\Delta(Z_p-Z_o)$ and $\Delta(Z_s-Z_o)$ are less than 3 nm and 39 nm , respectively. These results make clear that the values Z_p has a higher noise resistant and provides a higher accuracy in surface profile measurement.

Table 4.3. Differences in Z_s-Z_o and Z_p-Z_o between Table 4.1 and Table 4.2.

l_ε (μm)	0	10	20	30	40
$\Delta(Z_s-Z_o)$ (nm)	-15	29	-17	-39	29
$\Delta(Z_p-Z_o)$ (nm)	2	-1	3	3	-2

Finally, the simulation was carried out for different noise at $l_\varepsilon=40 \mu\text{m}$, as shown in Table 4.4. Noise I was used in Table 4.2. The averages and variances of three noises were the same. These noises produced different values of a_0 and a_1 . The difference in the values of Z_s-Z_o among the three noises was less than 55 nm. On the other hand, the difference in the values of Z_p-Z_o among the three noises is less than 2 nm. The conclusions obtained from Table 4.2 do not change for different noises, and the values Z_p provides a high repeatability in surface profile measurement.

Table 4.4. Simulation results for different noises at $l_\varepsilon=40 \mu\text{m}$.

$\varphi_n(z)$	a_0 (rad)	a_1 (rad μm)	Z_s-Z_o (μm)	Z_p-Z_o (μm)
Noise I	-280.721	270.052	-21.490	-21.596
Noise II	-287.446	270.324	-21.512	-21.594
Noise III	-282.214	271.023	-21.567	-21.595

4.4 Experiment

A white light scanning interferometer was constructed as shown in Fig. 4.1. The object was a glass with a step of 3 μm width on the surface. The reference surface was a glass with a wedge angle, and it was regarded as one reflecting surface. The inclination of the reference surface was adjusted so that the phase distribution of the interference pattern on the camera did not indicate a large inclination of the object surface which was caused by the distribution of the distance difference l_ε as shown in Table 4.1 and Table 4.2. The measuring points N_x was from 1 to 56, and N_y was from 1 to 41. The reference surface was moved by the PZT at a constant velocity of about 80 $\mu\text{m/s}$, and the sampling interval Δz of the interference signal was 39.6nm. The data number N of the detected signal was 1024, and required interference signal was selected with a rectangular window whose data number was 240. The other data outside the window were zero values. Figure 4.11 shows the windowed interference signal detected at a measurement point of $N_x=18$ and $N_y=18$, and the distance difference l_ε at this measurement point was about 45 μm . The interference signal indicates that the object position was about -1.23 μm . Although l_ε was equal to 88 μm at a measurement point $N_x=1$ and $N_y=18$, the object position indicated in the

interference signal was $-1.35 \mu\text{m}$. This fact means that the inclination of the surface profile caused by l_ε did not appear in the detected interference signal. Fourier transform was performed on the windowed interference signal, where the interval of wavenumber was $\Delta\sigma=1/(2N\Delta z)=0.0123\mu\text{m}^{-1}$. Figure 4.12 shows the phase of Fourier transform of the interference signal with blue color. The non-linear component of this phase distribution is almost similar as that in Fig. 4.9(b). The least squares line of the phase was shown by the red line. The values of a_0 and $a_1-4\pi Z_o$ were -24.357 rad and 19.715 rad $\cdot\mu\text{m}$, respectively. The measurement value Z_s obtained from $a_1-4\pi Z_o$ was $-1.569 \mu\text{m}$. Figure 4.13 shows the CVIS obtained by using the least squares line of the phase. The position Z_a was -1.571 nm and the measurement value Z_p was -1.609 nm.

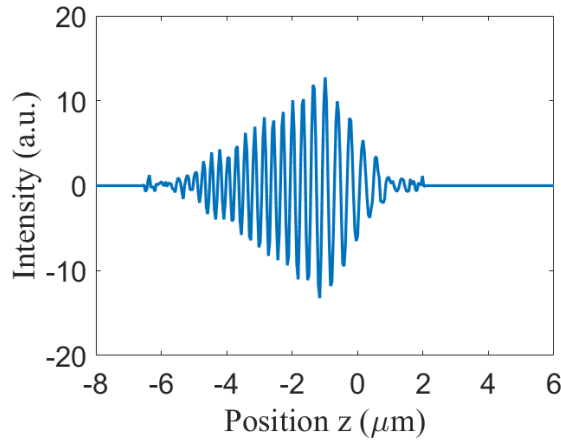


Fig. 4.11. Interference signal detected at measurement point of $N_x=18$ and $N_y=18$.

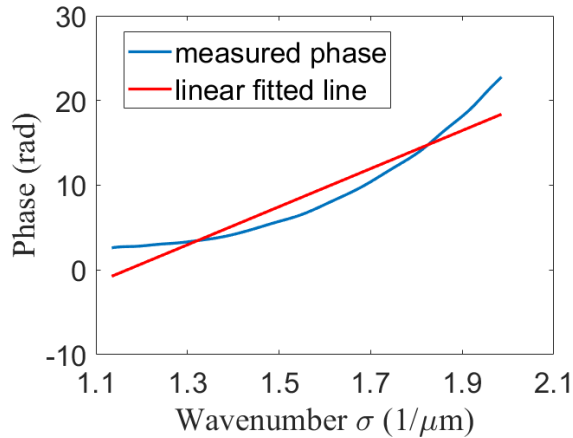


Fig. 4.12. Measured phase distribution of the interference in wavenumber domain and the least squares line of the distribution.

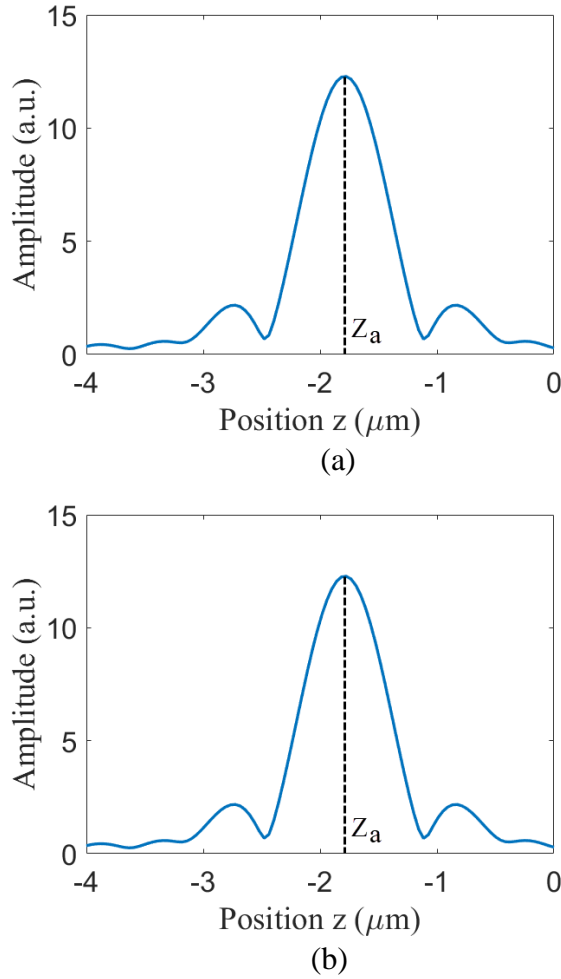


Fig. 4.13. Complex-valued interference signal of Fig. 4.11 obtained by using the least square line of the phase shown in Fig. 4.12. $Z_a = -1.583 \mu\text{m}$ and $Z_p = -1.609 \mu\text{m}$. (a) amplitude and (b) phase.

4.5 Measurement result

The signal processing to obtain the two measurement values of Z_s and Z_p was carried out for all of the measurement points to get surface profiles of the glass with the step shape. A surface profile obtained from the measured values of Z_s is shown in Fig. 4.14, where the tilt and piston component were eliminated. In order to show clearly the small variations in the surface profile, the surface profile on the left part in Fig. 4.14 is shown in Fig. 4.15. The magnitude of the small variations was less than 15 nm. Figure 4.16 shows the surface profile obtained from the measured values of Z_p . The surface profile on the left part in Fig. 4.16 is shown in Fig. 4.17. The measured surface profile was very smooth, and the magnitude of the small variations was less than 4 nm. The repeatability was obtained by calculating a root-mean-square value of the difference between two surface profiles measured in an interval of about 10 minutes. The repeatability was 1.3 nm

in the measurement by Z_p , while it was 13.3 nm in the measurement by Z_s . The step width between $N_x=34$ and $N_x=37$ along $N_y=28$ was 2.932 μm by the measured values of Z_p . It was made clear that the measurement value Z_p provides a more exact position of a measured reflecting surface than the measurement value Z_s .

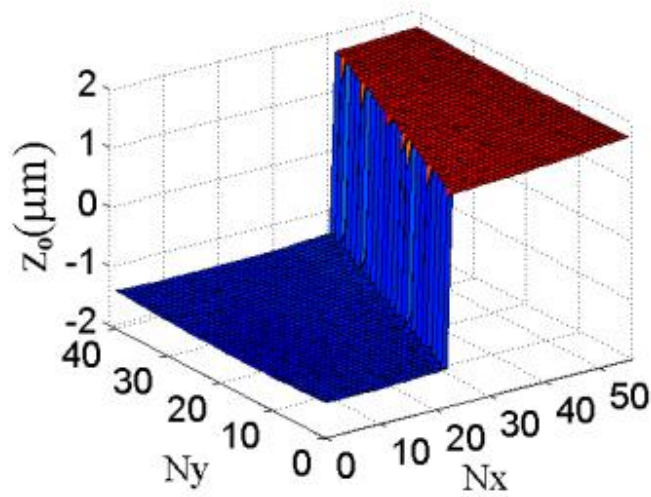


Fig. 4.14. Surface profile obtained from the measured values of Z_s .

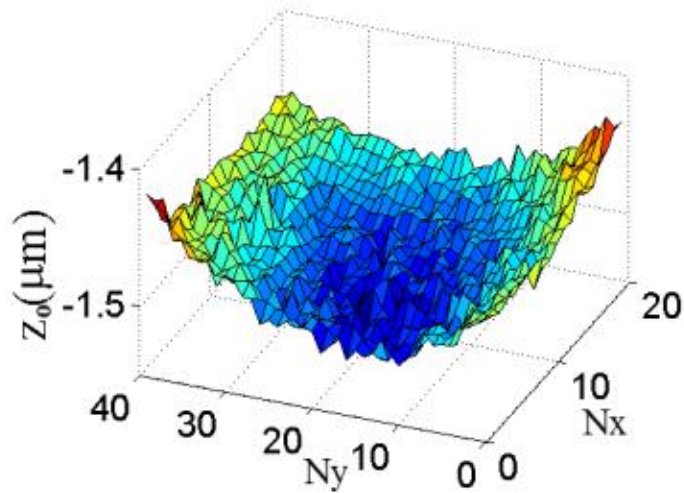


Fig. 4.15. Surface profile on the left part in Fig. 4.14.

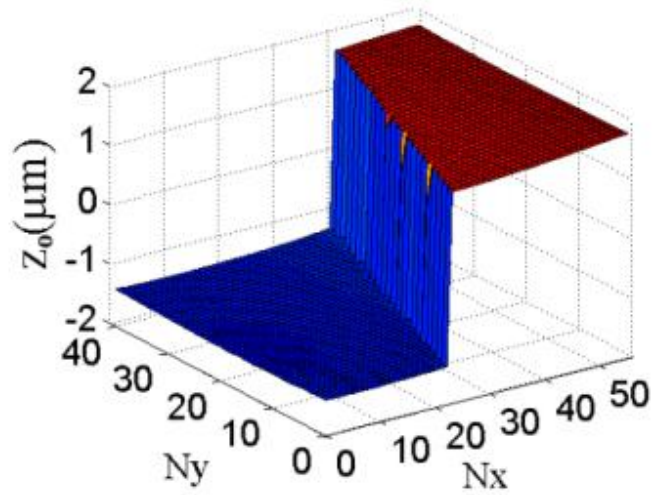


Fig. 4.16. Surface profile obtained from the measured values of Z_p .

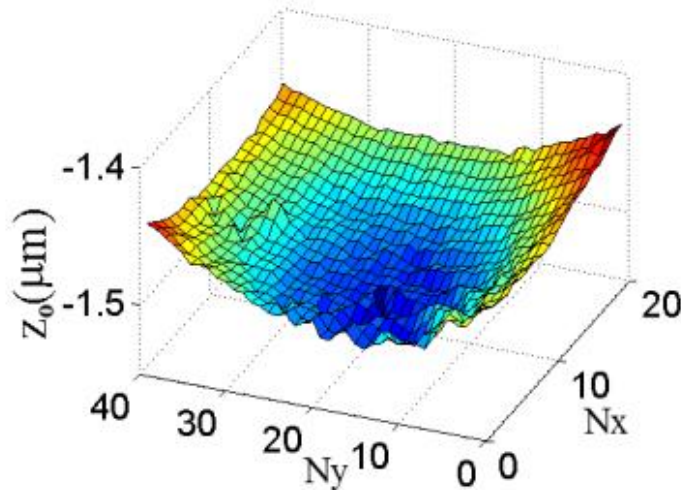


Fig. 4.17. Surface profile on the left side in Fig. 4.16.

4.6 Conclusion

The simulation results agreed with the equations described in principle and made clear the characteristics of the proposed signal processing. The existence of the dispersion phase leads to the result that the values of a_1 and a_0 change linearly with increase in the distance difference l_e . This distribution of the value a_1 produces an inclination of a surface profile in the direction of the x axis along which the magnitude of the dispersion phase changes linearly. But this inclination of the surface profile can be eliminated by adjusting the inclination of the reference surface in experiments. The changes in the values of a_1 and a_0 caused by the random phase noise generate a large measurement error less than 15 nm in the value Z_s , but the changes do not generate such a large measurement error in the value Z_p .

These characteristics of the proposed signal processing without using a measured dispersion phase lead to a high accurate measurement by the value Z_p with an error less than 4 nm.

CHAPTER 5

INTERFERENCE SIGNAL CORRECTION BY DETECTION OF SCANNING POSITION

5.1 Introduction

Signal processing methods are proposed to eliminate the dispersion phase in the chapters 3 and 4. In order to increase the measurement accuracy, it is necessary to consider the noise in WLSI. One kind of noise is additive noise such as the background light and the current noise of camera. And the other kind of noise is random noise caused by the vibration of optical component and the non-linear movement of PZT. The random noise has a bad influence on the OPD of interference signal. In this chapter the two interfering beams in the WLSI can be utilized to detect the time-varying OPD since a supercontinuum light source for the WLSI has a strong power. A beam-splitter is put in front of a camera for the WLSI in order to divide the two beams of the WLSI for the laser interferometer, and an optical band-pass filter is put in front of a photodiode to detect the signal of the laser interferometer. The time-varying OPD or the scanning positions can be easily and exactly obtained from this interference signal through the same signal processing as that of the WLSI. The calculated scanning positions are assigned to the corresponding sampling points of the interference signal detected in the WLSI. Since the sampling interval in the interference signal corrected with the calculated scanning positions is not constant, the interpolation is performed on corrected interference signal to obtain the interference signal with a constant sampling interval. This correction method for the scanning position leads to elimination of the non-constant movement of the PZT completely and the random noise caused by the external disturbances. These characteristics are made clearly by simulations. In experiments a surface profile with a step shape of 3 μm -height is measured accurately with an error less than 2 nm.

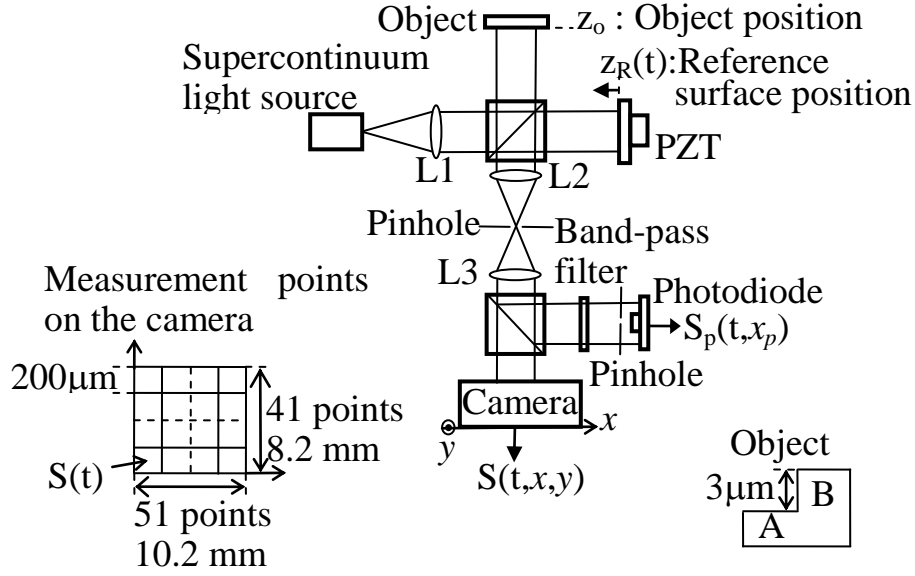


Fig. 5.1. Schematic of a white-light scanning interferometer.

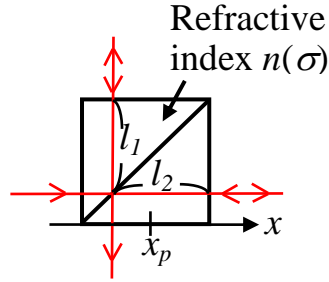


Fig. 5.2. Generation of dispersion phase by the distance difference of $l_e = l_2 - l_1$ in BS1. The beams at the position x_p are going to a photodiode.

5.2 Principle

Figure 5.1 shows a WLSI whose part to generated the interference signal (above the L3) is same with Fig. 3.1. The position of a reference surface is denoted by $z_R(t)$ which is changed by a piezoelectric transducer (PZT) with time t . Although the measurement points of the camera are on x-y plane, equations are described only on the x-axis for the sake of simplicity. Denoting the scanning position by $z(t)$, an interference signal detected on the measurement point of the camera is expressed as

$$S(t, x) = \int_{-\infty}^{\infty} I(\sigma) \cos\{4\pi[z(t) - z_o(x)]\sigma + \varphi_d(\sigma, x)\} d\sigma + n_A(t), \quad (5.1)$$

where the scanning position is given by

$$z(t) = z_R(t) + z_n(t) = V_a t + z_v(t) + z_n(t). \quad (5.2)$$

The scanning position contains the two following components: one is the reference surface position $z_R(t)$ which consists of a constant speed V_a and non-linear movement $z_v(t)$ of the PZT, and the other one is a random change $z_n(t)$ generated by external disturbances in the interferometer. The $n_A(t)$ is additive noise. The phase $\varphi_d(\sigma, x)$ is dispersion phase generated by the BS1, where the position x is the two beams go out from the beam splitter. The beams at the position x_p are going to a photodiode. The dispersion phase is given by

$$\varphi_d(\sigma, x) = 4\pi n(\sigma)l_\varepsilon(x)\sigma, \quad (5.3)$$

The beams are divided by the BS2 in front of the camera and the reflected beams are passed through a band-pass filter with the transmission wavenumber σ_f . The photodiode receives the beams coming from the position of $x=x_p$ on the BS1 with a pinhole, as shown in Figs. 5.1 and 5.2. An interference signal detected with the photodiode is expressed as

$$S_p(t, x_p) = I(\sigma_f) \cos\{4\pi[z(t) - z_o(x_p)]\sigma_f + \varphi_d(\sigma_f)\}. \quad (5.4)$$

The additive noise in $S_p(t, x_p)$ is ignored because the additive noise generated in the photodiode is very weak compared with the $n_A(t)$ generated in the camera and causes a very small error in calculated position value. In order to get a wrapped phase distribution of $S_p(t, x_p)$, inverse Fourier transform is performed on the distribution in positive frequency region of the Fourier transform of $S_p(t, x_p)$. After obtaining an unwrapped phase of $S_p(t, x_p)$, the phase is divided by $4\pi\sigma_f$ to obtain position value $z_c(t)$ which is given by

$$z_c(t) = z(t) - z_o(x_p) + z_b, \quad (5.5)$$

where $z_b=n(\sigma_f)l_\varepsilon(x_p)$ with Eq. (5.3). This scanning position value enables the conversion of the time in the signal $S(t)$ to the scanning position $z_c(t)$. Thus a corrected interference signal is obtained as

$$S(z_c, x) = \int_{-\infty}^{\infty} I(\sigma) \cos[4\pi(z_c - z_o(x) + z_o(x_p) - z_b)\sigma + \varphi_d(\sigma)]d\sigma + n_{AC}(z_c). \quad (5.6)$$

where the $n_{AC}(z_c)$ is the additive noise converted from $n_A(t)$. The effects of non-constant movement of the PZT and the random phase changes are eliminated in the corrected signal $S(z_c, x)$. If the dispersion phase $\varphi_d(\sigma)$ is equal to zero, the peak position of the interference signal appears at $z_c = z_o(x) - z_o(x_p) + z_b$. There is a constant shift of the peak position of $-z_o(x_p) + z_b$ which produces parallel displacement in a measured surface. But this displacement does not give any influence for surface profile measurement, because the measured position of a surface is a relative value in an interferometer. Hereafter the constant shift is ignored.

Figure 5.3 shows how the corrected signal $S(z_c)$ is obtained from the detected signal $S(t)$. The blue curve is the position value of $z_c(t) = z(t) - z_o(x_p) + z_b$ obtained from the interference signal $S_p(t)$. Small circle denotes the sampling time, and the value of $z_c(t)$ corresponding to the sampling time is indicated with small triangle. The value of the signal $S(t)$ detected at the sampling time is indicated with small square. This sampled value of $S(t)$ corresponds to the position value $z_c(t)$, which becomes to the value of the horizontal axis in the corrected signal $S(z_c)$. Thus this correspondence makes the corrected signal $S(z_c)$. Since the interval between the adjacent sampling points of the interference signal $S(z_c)$ is not constant, interpolation is carried out to get the interference signal whose sampling interval is constant.

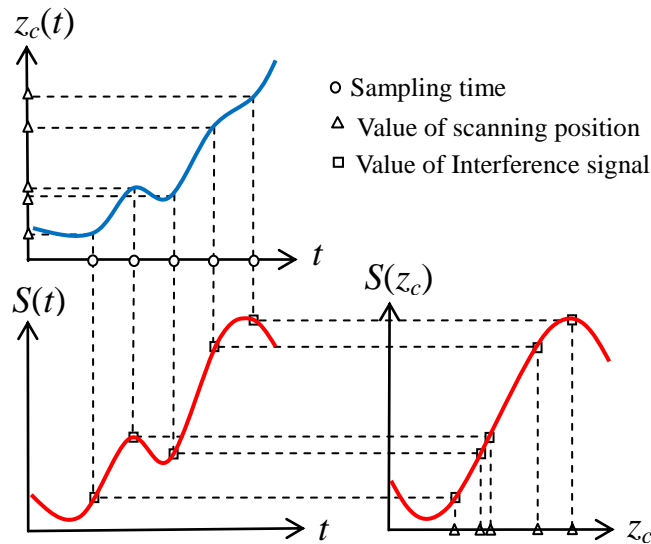


Fig. 5.3. Correction of the detected signal $S(t)$ by detection of the position value $z_c(t)$.

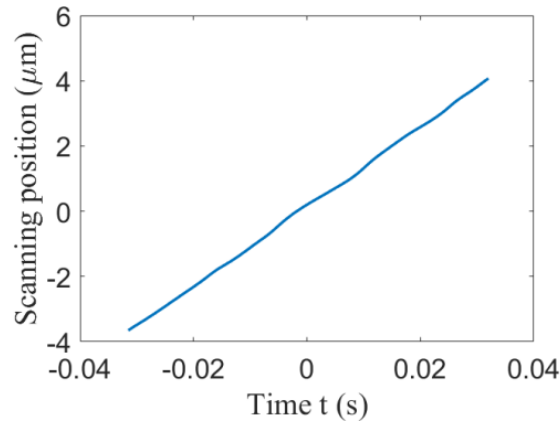
This corrected interference signal with a constant sampling interval is processed to get the object position Z_o with the signal processing explained in chapter 4. A position of maximum amplitude in the CVIS is denoted as Z_a .

The position Z_p of zero phase nearest to the position Z_a in the CVIS is the measurement value of Z_o . The measurement value Z_p in the corrected signal $S(z_c)$ is expected to provide a high measurement accuracy, which is verified by simulations and experiments in the following sections.

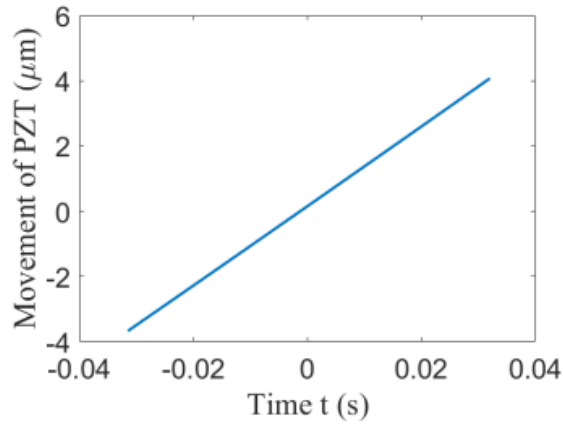
5.3 Detection of the scanning position and its components

The process to obtain the real scanning position value $z_c(t)$ from $S_p(t, x_p)$ is explained in details. In order to prevent the leakage effect in Fourier transform, a Gaussian window was used for $S_p(t, x_p)$. Fourier transform was performed on the windowed $S_p(t, x_p)$ whose data number N and the interval of Δt were 128 and 0.5 ms. The wrapped phase of $S_p(t, x_p)$ was obtained by performing inverse Fourier transform on the positive frequency components of the Fourier transform of $S_p(t, x_p)$. The start region of the unwrapping for the wrapped phase of $S_p(t, x_p)$ contained the maximum value point of $S(t)$. The time on the middle sampling point was regarded as $t=0$ s. Figure 5.4(a) shows the unwrapped phase of $z_c(t)$.

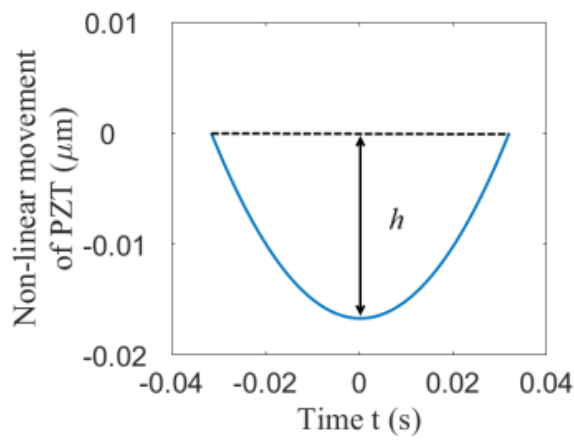
Assuming that the PZT moves with a constant acceleration, the movement of the PZT is expressed by a quadratic function $z_R(t) = at^2 + bt + c$. The movement $z_R(t)$ of the PZT was obtained from second-order polynomial fitting of $z_c(t)$ as shown in Fig. 5.4(b). The value of b was the average velocity V_a of the PZT, and it was equal to $60.98 \mu\text{m/s}$. The non-linear component $z_v(t)$ was equal to $at^2 + h$, where $a = 16.56 \mu\text{m/s}^2$. The value of h is decided from the condition that $z_v(t) = 0$ at the first sampling point. The depth h of $z_v(t)$ was 16.7 nm as shown in Figure 5.4(c). The random movement $z_n(t)$ obtained by subtracting the $z_R(t)$ from the $z_c(t)$ is shown in Fig. 5.4(d), where its standard deviation σ_n was 36.0 nm . In simulations, the distributions of $V_a t$, $z_v(t)$, and $z_n(t)$ with different values of h and σ_n are used to generate the interference signal.



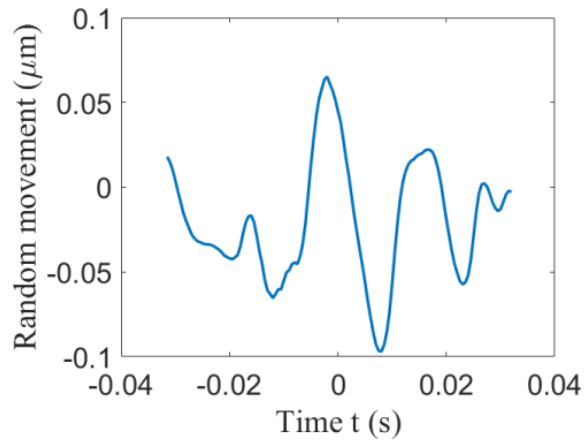
(a)



(b)



(c)



(d)

Fig. 5.4. (a) Scanning position $z_c(t)$ obtained from $S_p(t)$. (b) Movement $z_R(t)$ of the PZT obtained by second-order polynomial fitting. (c) Non-linear movement $z_v(t)$ of the PZT with $h=16.7$ nm. (d) Random movement $z_n(t)$ with $\sigma_n=36.0$ nm.

5.4 Simulation of effect of different phase error

It is explained how the interference signals were generated. The different magnitude of dispersion phase along x direction expressed by Eq.(5.3) brings an inclination along x direction to the measurement value Z_p described in chapter 4. Therefore it is reasonable to ignore the dispersion phase in the simulation for discussing effects of the non-linear movement of PZT, the random movement, and the additive noise. The interference signal given by Eqs.(5.1) and (5.4) were generated without $\varphi_d(\sigma)$. Figure 5.5 shows the spectrum $I(\sigma)$ of the supercontinuum light source detected with a spectral analyzer. Figure 5.6 shows the additive noise $n_A(t)$ obtained from experimental data, whose mean value is zero and standard variation is 0.11. The data of $z_c(t)$ in Fig. 5.4(a) were used as $z(t)$ in Eqs. (5.1) and (5.4) to generate the interference signal $S(t)$ and $S_p(t)$, and the object position z_o was equal to zero. The interference signal $S(t)$ scanned by $z(t)$ is shown in Fig. 5.7, where the additive noise $n_A(t)$ of Fig. 5.6 was contained with SNR (signal-noise ratio)=10.1. It is a general method that the horizontal axis t of $S(t)$ is regarded to have a relation of $z(t)=V_a t$ under the assumption that the PZT moved with a constant speed V_a . This interference signal is denoted by $S(z)$, where $z=60.98t \mu\text{m}$. In our method the detected interference signal $S(t)$ of Fig. 5.7 was corrected by using the scanning position $z_c(t)$ and cubic spline interpolation. This corrected interference signal $S(z_c)$ is shown in Fig. 5.8, where the period of the sinusoidal waveform becomes almost constant. It will be shown below that the measurement error in the corrected interference signal is less than a few nanometers.

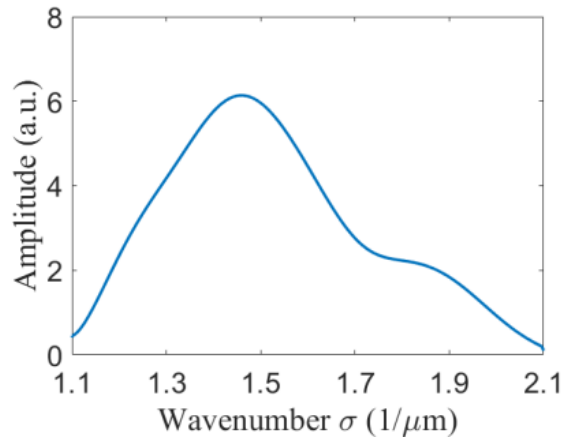


Fig. 5.5. Spectrum $I(\sigma)$ of the light source.

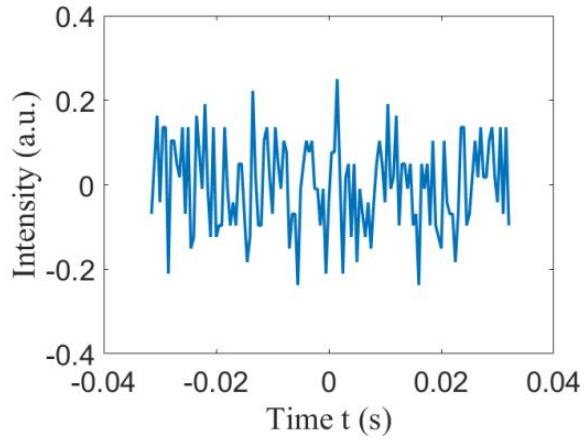


Fig. 5.6. Additive noise $n_A(t)$.

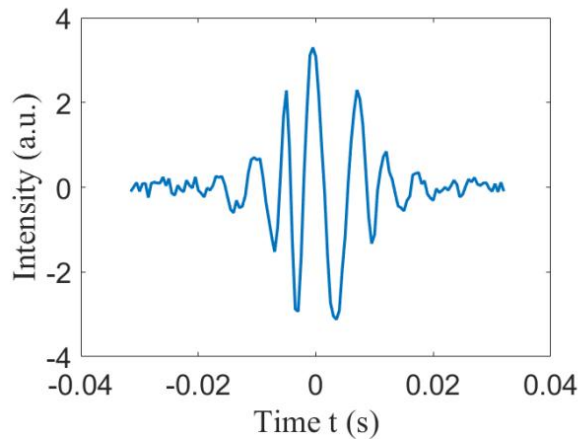


Fig. 5.7. Interference signal $S(t)$ scanned by $z(t)$.

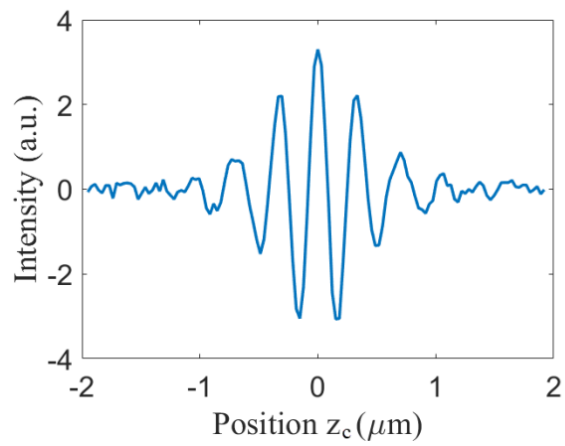


Fig. 5.8. Interference signal corrected by the scanning position $z_c(t)$.

5.4.1 Effect of the non-linear movement of PZT

It was investigated how much the non-linear movement $z_v(t)$ of the PZT causes the measurement error of Z_p-Z_o . In this case the scanning position was $z(t)=V_d t+z_v(t)$ with different values of h , and the random movement $z_n(t)$ and the additive noise $n_A(t)$ were equal to zero. Table 5.1 shows the measurement errors in the detected signal $S(z)$ and the corrected signal $S(z_c)$, respectively. The measurement error in $S(z)$ changes linearly with the increase of h . On the other hand, magnitude of the error in $S(z_c)$ is always less than 0.04 nm regardless of the values of h . Therefore it was made clear that the correction of the interference signal by $z_c(t)$ could eliminate completely the measurement error caused by the non-linear movement of the PZT.

Table 5.1. Measurement errors caused by $z_v(t)$ in $S(z)$ and $S(z_c)$.

h (nm)	10	20	30
Error in $S(z)$ (nm)	10.1	20.2	30.3
Error in $S(z_c)$ (nm)	0.04	0.03	0.04

5.4.2 Effect of the random movement

In order to investigate effects of the random movement $z_n(t)$, the scanning position was $z(t)=V_d t+z_v(t)+z_n(t)$ with $h=20$ nm because of $h=16.7$ nm in the experimental data. The additive noise $n_A(t)$ was equal to zero. A mean value (MV) and a standard deviation (SD) of the measurement error caused by the random movement were calculated by using six different samples of noise $z_n(t)$ with a same standard deviation σ_n . Table 5.2 shows the measurement errors with different values of the standard deviation σ_n in $S(z)$ and $S(z_c)$. The MV of the error in $S(z)$ was dozens of nanometers and became larger as the increase of the standard deviation σ_n . The MV of the error in $S(z_c)$ was in the range from 0.03 to 0.54 nm, and the SD was almost equal to the MV. It was clear that the measurement error caused by $z_n(t)$ could be eliminated in $S(z_c)$ and the MV of the error are less than 0.5 nm in the region less than $\sigma_n=60$ nm.

Table 5.2. Measurement errors caused by $z_n(t)$ at $h=20$ nm in $S(t)$ and $S(z_c)$.

σ_n (nm)	20	40	60
MV of error in $S(z)$ (nm)	21.4	32.8	49.9
MV of error in $S(z_c)$ (nm)	0.03	0.18	0.54
SD of error in $S(z_c)$ (nm)	0.03	0.14	0.51

5.4.3 Effect of the additive noise

Finally, the interference signal $S(t)$ contained the additive noise $n_A(t)$, and the scanning position was $z(t)=V_a t+z_v(t)+z_n(t)$ with $h=20$ nm and $\sigma_n=40$ nm. SNR of the interference signal was defined as the ratio between the SDs of $S(t)$ and $n_A(t)$. The calculated measurement errors at different values of SNR are shown in Table 3. The MVs in $S(z_c)$ in Table 5.3 are very larger than those at $\sigma_n=40$ nm in Table 5.2.

Table 5.3. Measurement errors caused by $n_A(t)$ at $h=20$ nm and $\sigma_n=40$ nm in $S(t)$ and $S(z_c)$.

SNR	20	10	5
MV of error in $S(z)$ (nm)	32.0	32.4	33.8
MV of error in $S(z_c)$ (nm)	0.63	1.17	2.28
SD of error in $S(z_c)$ (nm)	0.40	0.70	1.36

The measurement error by the non-linear movement of the PZT is very small comparing the errors caused by $z_n(t)$ and $n_A(t)$. Therefore, the non-linear movement of the PZT does not give any effect on the measurement error in $S(z_c)$. The measurement errors by $z_n(t)$ are much smaller than those by $n_A(t)$ in $S(z_c)$ and the measurement error caused mainly by $n_A(t)$ is less than 2 nm in the actual experimental conditions.

5.5 Experiment

The WLSI shown in Fig. 5.1 was constructed. The object was a glass plate having two surfaces with a step of 3 μm height, and the two surfaces of object were denoted by A and B. The reference surface was a glass plate with a wedge angle, and the glass plate was regarded as one reflecting surface. The average speed of reference mirror was 61 $\mu\text{m/s}$. In order to make the measurement points with interval of 200 μm , an interference signal detected on one pixel of camera was selected every 10 pixels along x and y directions. N_x was from 1 to 51, and N_y was from 1 to 41. Central wavelength and bandwidth of the band-pass filter were 633 nm and 3 nm, respectively. The interference signal $S_p(t)$ detected with the photodiode was transferred to a computer with an A-D converter. A start trigger and an external sampling clock of 2 KHz were provided to the high-speed camera and the A-D converter to capture the interference signals. The number of the sampling points of the $S_p(t)$ and $S(t)$ was 1024. Figure 5.9(a) shows the interference signal $S_p(t)$ whose average period and full width at half maximum are about 5 ms and 65 μm , respectively. Figure 5.9(b) shows the

sum of the non-linear movement $z_v(t)$ and the random movement $z_n(t)$ containing in the scanning position $z_c(t)$ obtained from $S_p(t)$. Figure 5.10(a) shows the interference signal $S(t)$ detected on a measurement point of $N_x=10$ and $N_y=20$ at the surface A. The interference signal $S(z_c)$ corrected by the scanning position $z_c(t)$ is shown in Fig. 5.10(b). It is shown clearly that the corrected signal $S(z_c)$ consists of a sinusoidal wave form with an almost constant period compared to the signal $S(t)$.

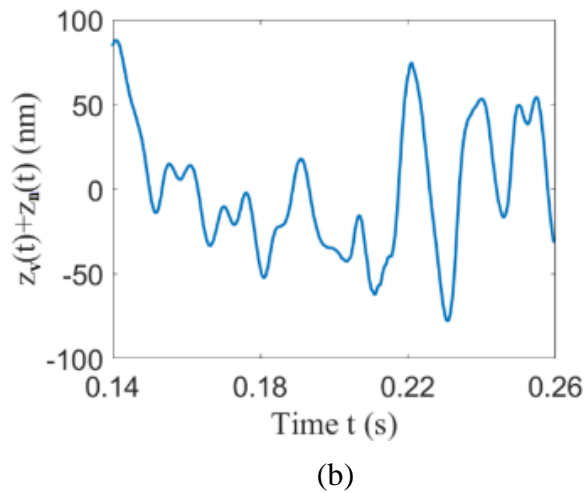
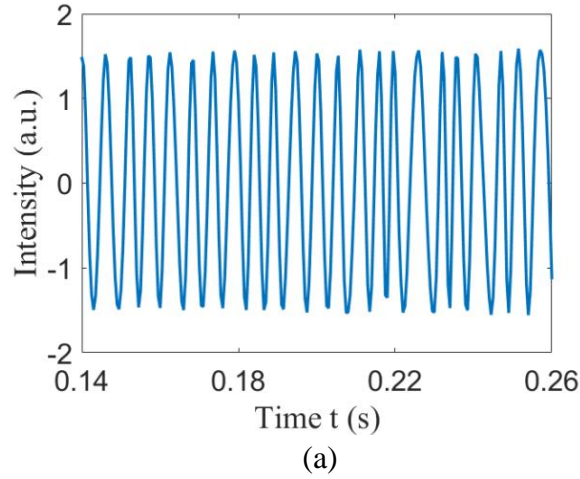


Fig. 5.9. (a) Interference signal $S_p(t)$ detected with the photodiode. (b) Sum of the non-linear movement $z_v(t)$ and the random movement $z_n(t)$ containing in the scanning position $z_c(t)$ obtained from the $S_p(t)$.

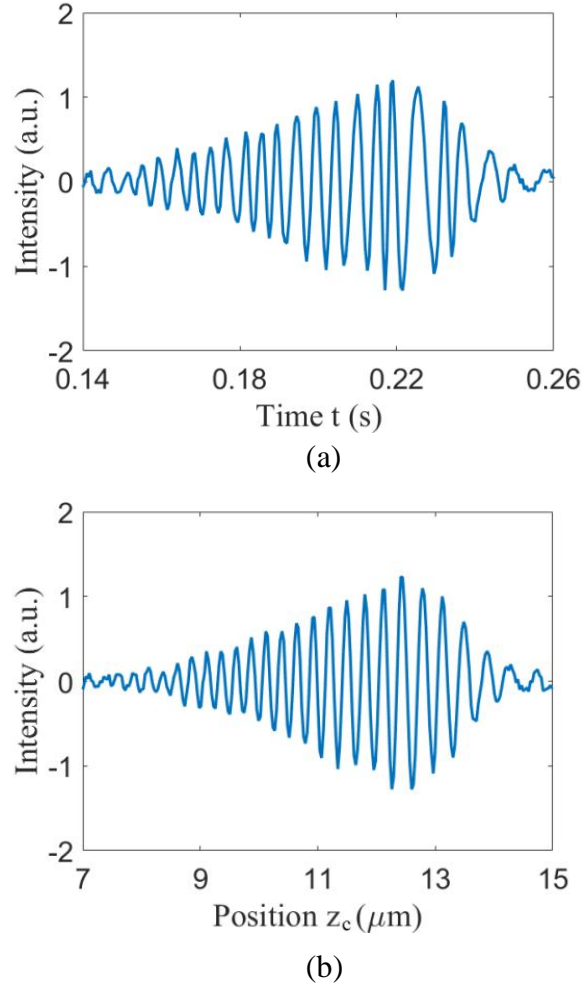
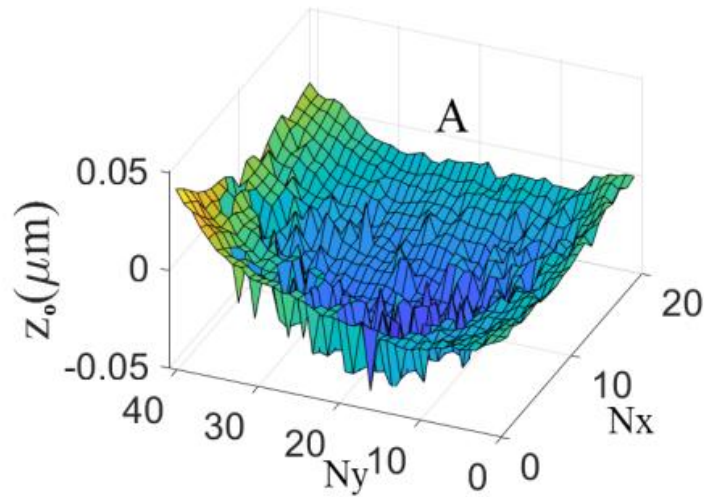


Fig. 5.10. (a) Interference signal $S(t)$ detected at a measurement point of $N_x=10$ and $N_y=20$. (b) Corrected interference signal $S(z_c)$.

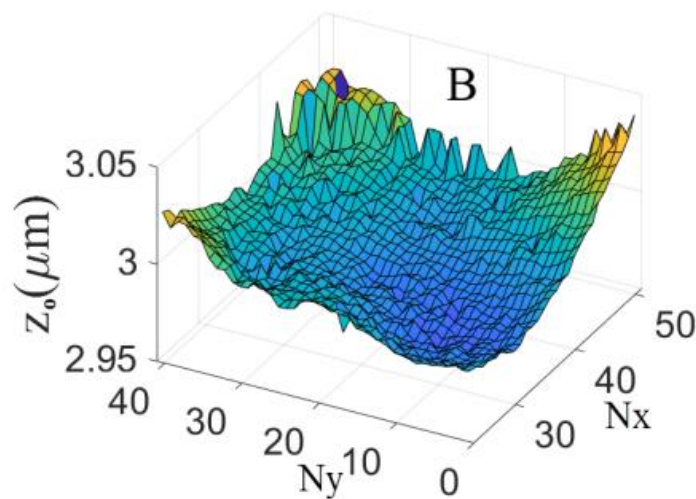
5.6 Measurement result

The signal processing to obtain the measurement value Z_p was carried out for all of the measurement points to get surface profiles of the object. The measurements were repeated three times at intervals of about 10 minutes. These measurements were called as M1, M2, and M3. The surface profile obtained from the signal $S(t)$ or $S(z)$ in M1 are shown in Figs. 5.11(a) and (b), where the tilt and piston components are eliminated. In order to show clearly the small variations, surface A and B are shown separately. The step height between the two surfaces was 2.839 μm as shown in Fig. 5.12. Figure 5.13 shows one-dimensional surface profiles at $N_x=10$ obtained from $S(z)$ in the three measurements. SD of $z_n(t)$ were 30.9 nm in M1, 7.6 nm in M2, and 21.5 nm in M3. The repeatability of the profiles on surface A and surface B were 6.0 nm and 6.2 nm, respectively. The magnitude of the small variations on the two surfaces was less than 30 nm.

Next, the corrected signal $S(z_c)$ was used for the three measurements of M1 to M3. The profiles of surface A and surface B obtained from the $S(z_c)$ in M1 are shown in Figs. 5.14(a) and (b), respectively. The measured step height was $2.963 \mu\text{m}$ as shown in Fig. 5.15. This measured value was consistent with the nominal values of $2.95\text{-}3.05 \mu\text{m}$ caused by an error of the manufacture. Figure 5.16 shows one-dimensional surface profiles at $N_x=10$ obtained from $S(z_c)$ in the three measurements. Compared with the distributions in Fig. 5.13, the three measurement results in Fig. 5.16 are almost same and the measurement repeatability of surface A and surface B is 0.5 nm and 0.6 nm , respectively. The magnitude of the small variations on the two surfaces was less than 2 nm . It was made clear that the interference signal corrected by the scanning position $z_c(t)$ provided a more exact measurement value Z_p for the surface profiles.



(a)



(b)

Fig. 5.11. Profiles of (a) surface A and (b) surface B obtained from $S(z)$.

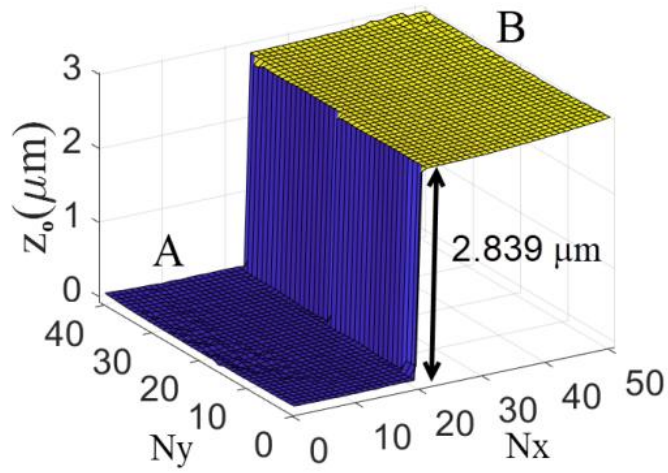


Fig. 5.12. Surface profile obtained from $S(z)$.

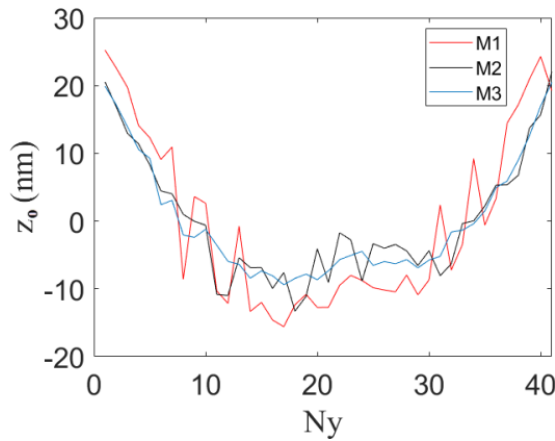
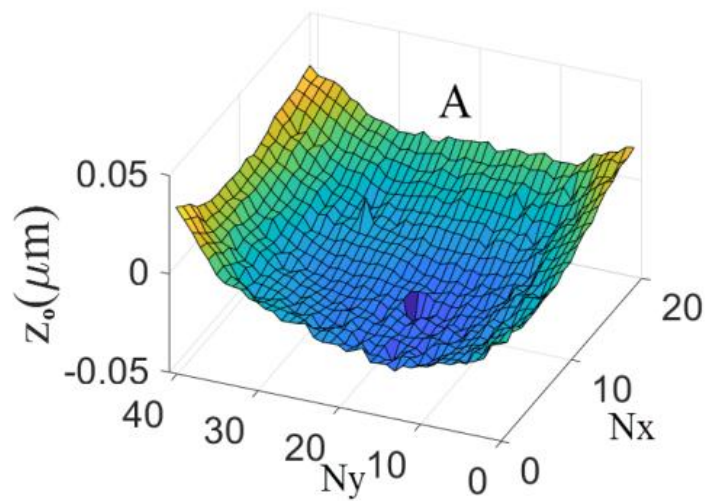


Fig. 5.13. One-dimensional surface profiles at $N_x=10$ obtained from $S(z)$ in the three measurements.



(a)

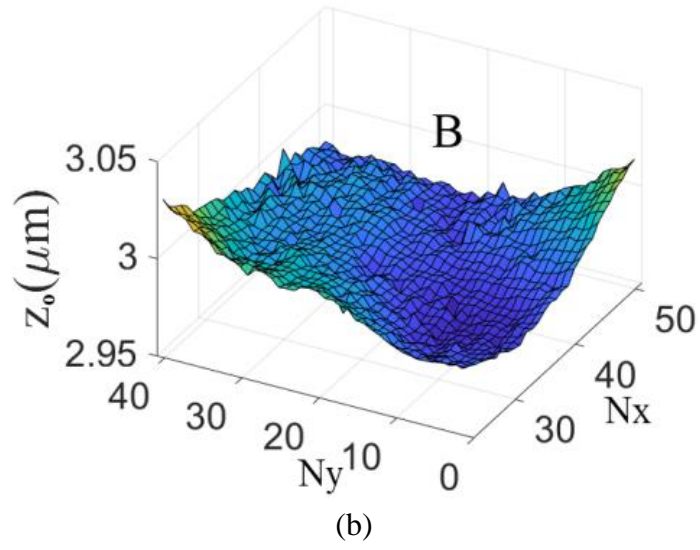


Fig. 5.14. Profiles of (a) surface A, and (b) surface B obtained from $S(z_c)$.

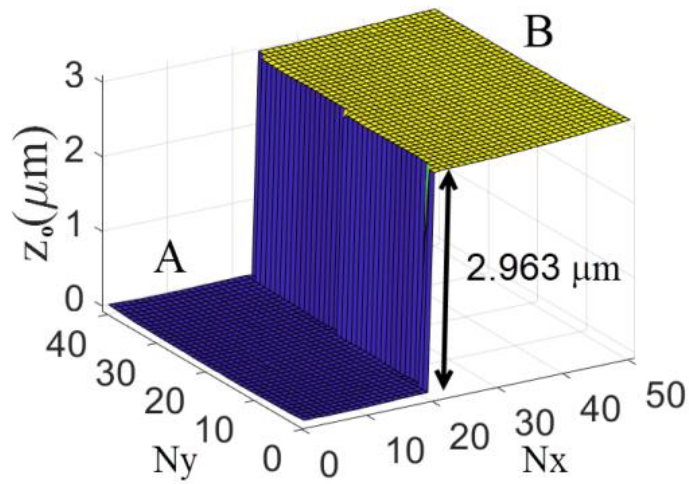


Fig. 5.15. Surface profile obtained from $S(z_c)$.

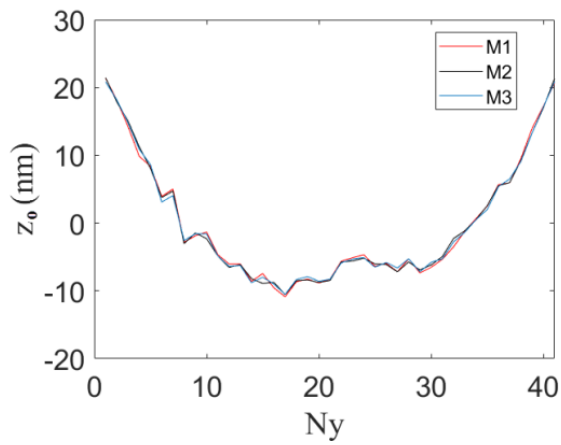


Fig. 5.16. One-dimensional surface profiles at $N_x=10$ obtained from $S(z_c)$ in the three measurements.

5.7 Conclusion

The additional interferometer was simply equipped in the WLSI by using the light source of the WLSI, the beam-splitter, the optical band-pass filter, and the photodiode without poorly influencing the WLSI. The actual OPD was easily calculated from the interference signal detected with the photodiode through the same signal processing as that in the WLSI. The scanning positions of the interference signal in the WLSI were corrected by the actual OPD values, and the corrected interference signal with a constant sampling interval is obtained by cubic spline interpolation. It was shown that the actual OPD or the scanning position changing with time contained the linear and non-linear movement of the PZT and the random movement by the external disturbances. It was clear in simulations that the non-linear movement did not cause any measurement error, and the random movement causes a small measurement error less than about 0.5 nm in the corrected interference signal. The additive noise contained in the interference signal of the WLSI caused a measurement error of a few nanometers in the simulations, which means that the additive noise is a main source of the measurement error after eliminating the measurement errors by the non-linear movement and the random movement. With the correction method a surface profile with a step shape of 3 μm -height was measured accurately with an error less than 2 nm.

CHAPTER 6

COMPENSATION OF DISPERSION EFFECT IN SHAPE MEASUREMENT OF THIN GLASS PLATE

6.1 Introduction

The chapters of 3,4,5 describe the researches to measure the surface profiles. The changing dispersion phase of BS along x direction generates the $\lambda_A/2$ position jumps on value of Z_p . After the eliminating the $\lambda_A/2$ position jumps, the inclination and bias does not have influence on the surface measurement. The inclination and bias after eliminating the $\lambda_A/2$ position jumps are important for measurement of thickness. When the value of Z_p is used to the measure the thickness of thin film, the dispersion phase generated by the thin film makes the $\lambda_A/2$ position jumps different between the front and rear surface. In this chapter, the coefficients to relate the Z_a and Z_p values to the actual thickness are determined by simulations. It is also made clear how at some thickness the Z_p value jumps by half of the weighted average wavelength in the light source. The number of occurrences of this position jump is obtained from the Z_a and Z_p values. An exact thickness measurement of a thin film can be achieved by using the coefficients and the number of occurrences of the position jump. Since measurement of a front surface profile of a thin film is the same as the measurement in chapter 4, the shape measurement is completed by combining the front surface profile and the thickness distribution.

6.2. Principle

6.2.1 Signals generated by front and rear surfaces

Figure 6.1 shows the interferometer with a light source whose spectral intensity is $I(\sigma)$, where σ is the wavenumber. A glass plate with two reflecting surfaces is an object to be measured. Thickness T is the distance between a front surface position Z_F and a rear surface position Z_R . The reference surface is a front surface of a glass plate with a wedge angle. Position z of the reference surface is scanned by a piezoelectric transducer (PZT). The interference $S(z)$ detected with a camera consists of two signals $S_F(z)$ and $S_R(z)$ which are generated by the beams reflected from the front and rear surfaces of the object, respectively, as shown in Fig. 6.2(a). Optical path length of the beam reflected from the rear surface is expressed as

$$Z_{RT}(\sigma) = Z_F + n(\sigma)(Z_R - Z_F) \quad , \quad (6.1)$$

where $n(\sigma)$ is the refractive index of the object. Since π phase change occurs in a beam which is reflected from a front surface of a glass plate and going back to air, the π phase appears in the signal $S_R(z)$. By ignoring the terms independent of the scanning position z , the interference signals are given by

$$S_F(z) = \int_{-\infty}^{\infty} I(\sigma) \cos[4\pi(z - Z_F)\sigma] d\sigma, \quad (6.2)$$

$$S_R(z) = \int_{-\infty}^{\infty} I(\sigma) \cos[4\pi(z - Z_{RT})\sigma + \pi] d\sigma. \quad (6.3)$$

The signal $S_F(z)$ has a maximum value at the position of $z=Z_F$. Since the signal $S_R(z)$ contains π phase, its maximum value is negative. Moreover, the maximum value of $S_R(z)$ appears around the rear surface position of Z_R because the Z_{RT} is a function of σ , as shown in Fig. 6.2(a). The signal processing method reported in chapter 4 is applied to the signals $S_F(z)$ and $S_R(z)$. A rectangular window is multiplied by the $S(z)$ to select the $S_F(z)$. Fourier transform is performed on $S_F(z)$ to obtain amplitude and wrapped phase distribution in wavenumber domain. Because the Z_F is constant value for all the wavenumbers when the beam splitter (BS) does not generate any dispersion effect, the unwrapped phase of $S_F(z)$ is a linear function of the wavenumber. Inverse Fourier transform is performed on the amplitude and phase distributions selected by the rectangular window as shown in Fig. 6.2(b), and a complex-valued interference signal (CVIS) of $S_F(z)$ is obtained as shown in Fig. 6.2(c). The maximum amplitude positions of CVIS of $S_F(z)$ is denoted as measurement value Z_{a1} , and the zero phase position nearest to Z_{a1} is denoted as measurement value Z_{p1} , as shown in Fig. 6.2(c). Here $Z_{a1}=Z_{p1}=Z_F$ without any dispersion effect. The same signal processing is performed on $S_R(z)$. Because of the dispersion phase generated by the glass plate, the unwrapped phase of Fourier transform of $S_R(z)$ has non-linear component in wavenumber domain. Least square line of this unwrapped phase is calculated as shown in Fig. 6.2(b). Inverse Fourier transform is performed by using this linear phase distribution to obtained the CVIS of $S_R(z)$. The maximum amplitude positions of $S_R(z)$ is denoted as measurement value Z_{a2} . The π phase position nearest to Z_{a2} is denoted as measurement value Z_{p2} . These measurement values do not directly provide the value of Z_R . The characteristics of Z_{a2} and Z_{p2} are examined in the following section by simulation. The period of phase distributions in the CVISs of $S_F(z)$ and $S_R(z)$

is $\lambda_A/2$. This λ_A value corresponds to the weighted average wavenumber σ_A in the spectral distribution $I(\sigma)$.

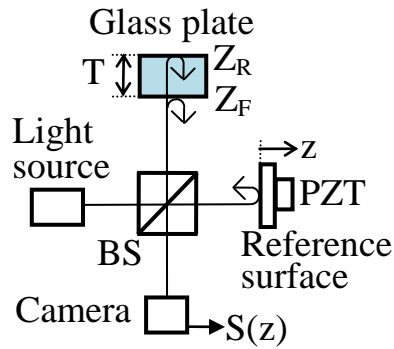
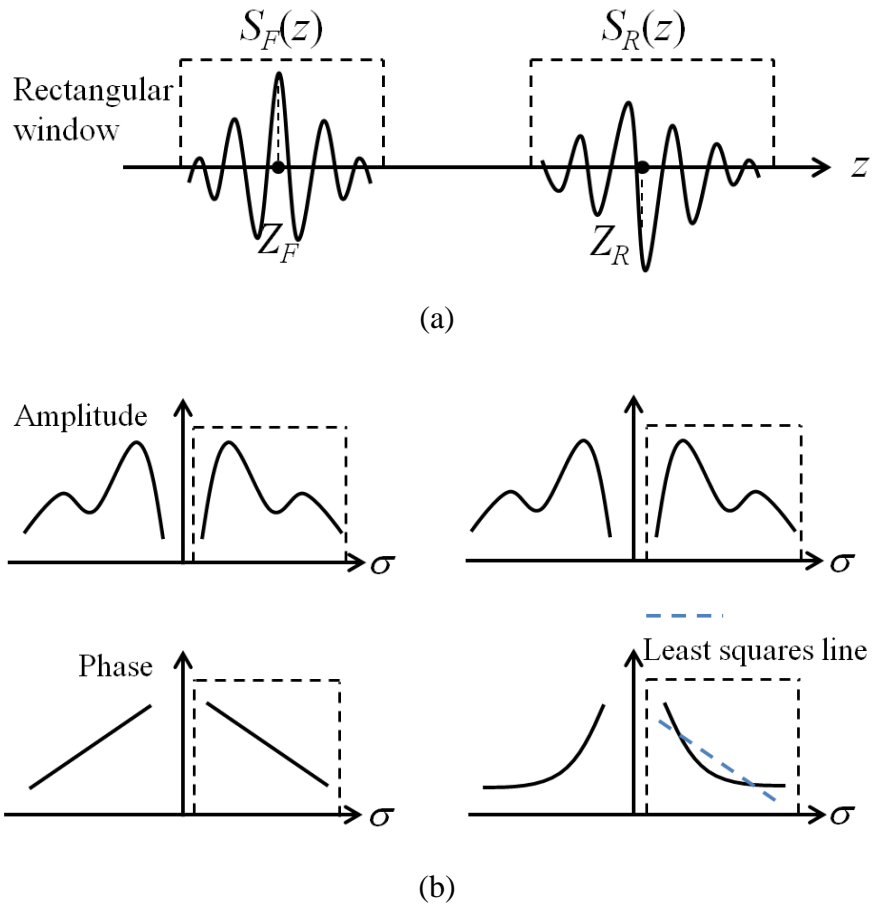


Fig. 6.1. Schematic of a white-light scanning interferometer for shape measurement.



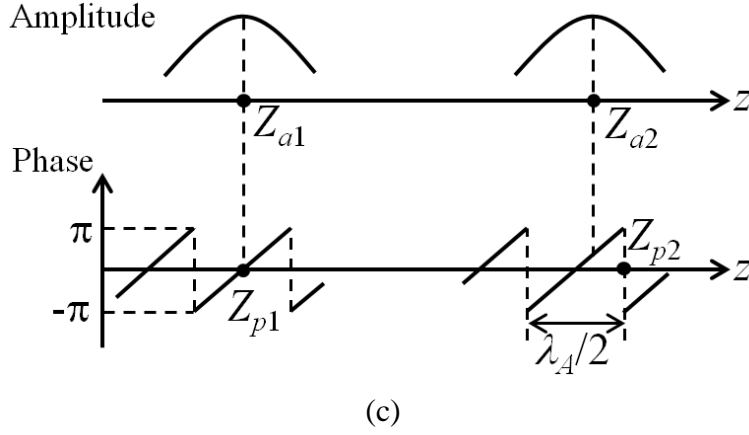


Fig. 6.2. (a) Interference signal $S(z)$ consisting of signals $S_F(z)$ and $S_R(z)$. (b) Fourier transform of $S_F(z)$ and $S_R(z)$. (c) Complex-valued interference signal of (a).

6.2.2. Characteristics of Z_{a2} and Z_{p2}

It was assumed for the sake of simplicity that $Z_{a1} = Z_{p1} = 0$, and the Z_{a2} and Z_{p2} were denoted by Z_a and Z_p . Then the signal of $S_R(z)$ for the simulation was given by

$$S_R(z) = \int_{-\infty}^{\infty} I(\sigma) \cos\{4\pi[z - n(\sigma)T]\sigma + \pi\} d\sigma, \quad (6.4)$$

where $T = Z_R - Z_F$. $I(\sigma)$ was an actual spectral intensity of the light source detected with a spectral analyzer, and $n(\sigma)$ was the formula of refractive index of BK7. The Z_a and Z_p values were obtained from the interference signal of Eq.(6.4) at T values from 1 μm to 100 μm . Figure 6.3 shows the Z_a and Z_p distributions at T values from 85.0 μm to 85.2 μm . Although the Z_a and Z_p values are proportional to T value, there is a position jump with a magnitude of $\lambda_A/2$ at $Z_p = 85.187 \mu\text{m}$. In order to show the characteristics of Z_a and Z_p distributions clearly, the schematic representation of the simulation results is shown in Fig. 6.4. The difference between Z_a and Z_p values increases as T value increases from zero at $Z_a = Z_p = 0$. Z_p value has a position jump with a magnitude of $\lambda_A/2$ when the distance d between Z_a and Z_p becomes $\lambda_A/4$. The reason why this position jump of Z_p occurs is that Z_p value is π phase position nearest to Z_a and the period of the phase distribution is $\lambda_A/2$ as shown in Fig. 6.2(c). The Z_a distribution is given by $Z_a = C_a T$. The Z_p distribution is given by $Z_p = C_p T + nj(\lambda_A/2)$, where nj is the number of occurrence of the jump. The values of C_a and C_p were 1.53612 and 1.51504, respectively. The λ_A was 0.653 μm . The position T_1 of the first position jump is obtained from the equation of $(C_a - C_p)T_1 = \lambda_A/4$, and $T_1 = 7.744 \mu\text{m}$. The interval ΔT_j of the position jumps is obtained from the equation of $(C_a - C_p)\Delta T_j = \lambda_A/2$, and $\Delta T_j = 15.489 \mu\text{m}$.

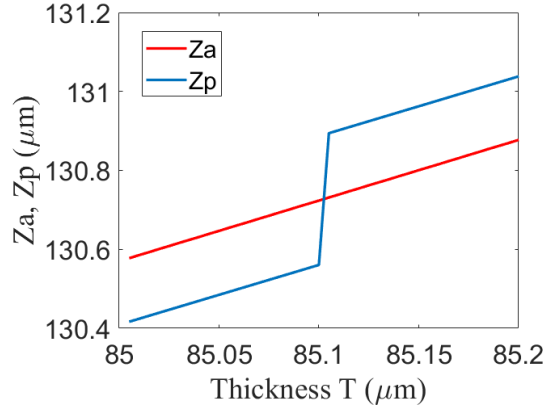


Fig. 6.3. The Z_a and Z_p distributions obtained from simulation.

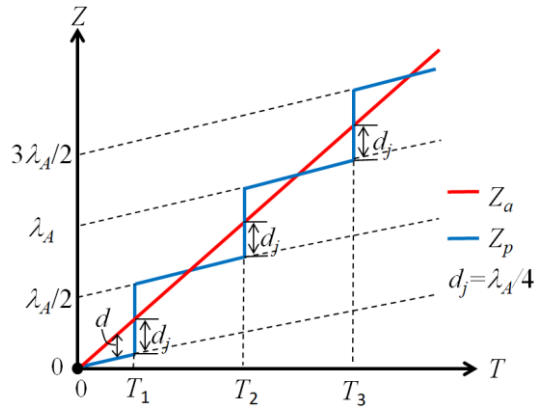


Fig. 6.4. Schematic representation of Z_a and Z_p distributions along glass thickness T .

6.2.3. Calculation of thickness

In experiment, the Z_{a1} was not equal to Z_{p1} because of the dispersion effect generated by the manufacturing error in the side length of the cubic BS1 in Fig. 6.5. The Z_{a2} and Z_{p2} also affected by the same dispersion effect of the BS. Because this dispersion effect produces a same measurement error on Z_{a1} and Z_{a2} , a value of $D_a = Z_{a2} - Z_{a1}$ is used to eliminate the dispersion effect. Also a value of $D_p = Z_{p2} - Z_{p1}$ is used. D_a and D_p related only to the thickness of glass plate are given by:

$$D_a = C_a T, \quad (6.5)$$

$$D_p = C_p T + nj(\lambda_A / 2), \quad (6.6)$$

From Eqs. (6.5) and (6.6), the nj is given by

$$nj = \frac{D_p - C_p (D_a / C_a)}{\lambda_A / 2}. \quad (6.7)$$

Since noises in experiments such as random vibrations of the optical components will produce measurement errors in the D_a and D_p values the nj calculated with Eq. (6.7) is not an integer value. The calculated value of nj is rounded off to an integer value. By using the integer value nj , the thickness T is obtained from Eq. (6.6) as follows:

$$T = \frac{D_p - nj(\lambda_A / 2)}{C_p}. \quad (6.8)$$

6.3 Experiment

6.3.1 Setup of interferometer and detected signals

A WLSI in Fig. 6.5 is similar with Fig. 6.1. The object was a thin glass plate whose thickness was in the region of 19-20 μm . The object and reference beams had different path distances of l_1 and l_2 in the BS1. An interference signal detected on one pixel was selected every 10 pixels along x and y direction. The measurement area was a circle with radius of 4 mm pixels and center of $N_x=20$, $N_y=20$. The speed of the PZT was not constant, and its average speed was 68.2 $\mu\text{m/s}$. The interval and the number of the sampling points of the $S_p(t)$ and $S(t)$ were 0.5 ms and 2048. Figure 6.6(a) shows the interference signal of $S(t)$ detected on a measurement point of $N_x=20$ and $N_y=20$. Non-linear movement of PZT and vibrations of optical component caused the non-linear change in the OPD. The other parameter is same with chapter 5. Figure 6.6(b) shows a part of $S_p(t)$ corresponding to $S_F(t)$ in the time region of 0.41-0.43 s, where two different periods existed. Figure 6.6(c) shows a part of $S_p(t)$ corresponding to $S_R(t)$. It is clear that the scanning position was not proportional to time. The signal correction method in chapter 6 was applied to eliminate the effect of non-linear change in the scanning positions of $S(t)$. The scanning position $z_c(t)$ was calculated from $S_p(t)$, and the $z_c(t)$ converted the sampling time t of the $S(t)$ to the corresponding scanning position z_c . After making interpolation for the converted signal $S(z_c)$, the interference signal $S(z_c)$ with a constant sampling interval was obtained as shown in Fig. 6.7. The interference signal $S_F(z_c)$ was asymmetry and its width was expanded to about 230 sample points because of the dispersion effect of BS1. Additional dispersion of the thin glass plate produced the $S_R(z_c)$ with width of about 280 sample points.

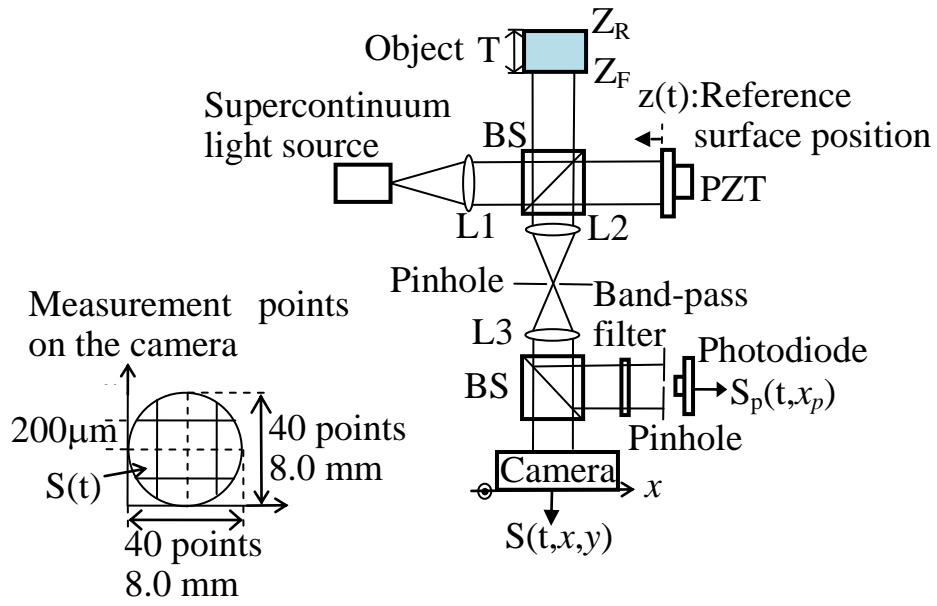


Fig. 6.5. Schematic of a white-light scanning interferometer with detection of the scanning positions.

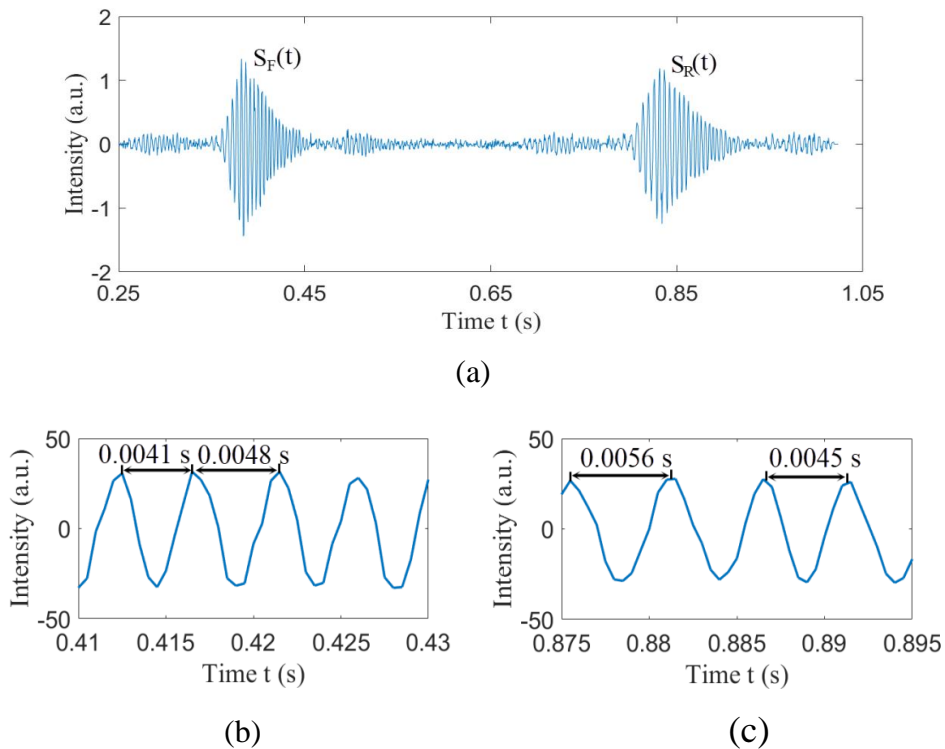


Fig. 6.6. Detected interference signals of $S(t)$ and $S_p(t)$. (a) $S_F(t)$ and $S_R(t)$ in the $S(t)$. (b) $S_p(t)$ corresponding to a part of $S_F(t)$. (c) $S_p(t)$ corresponding to a part of $S_R(t)$.

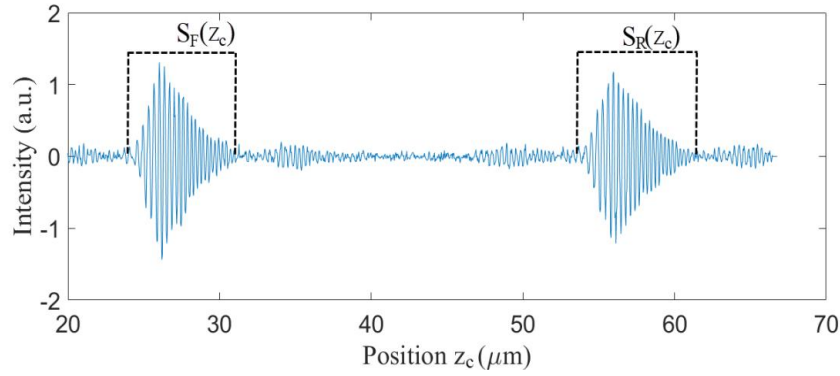
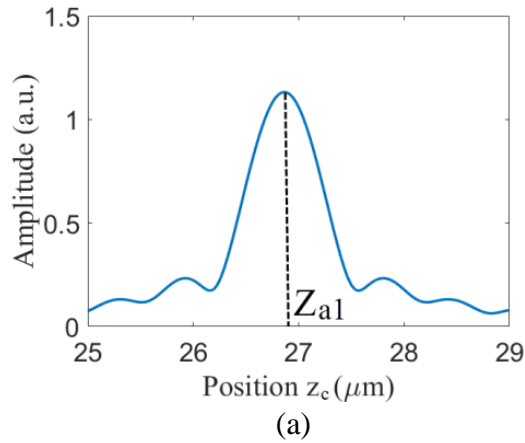
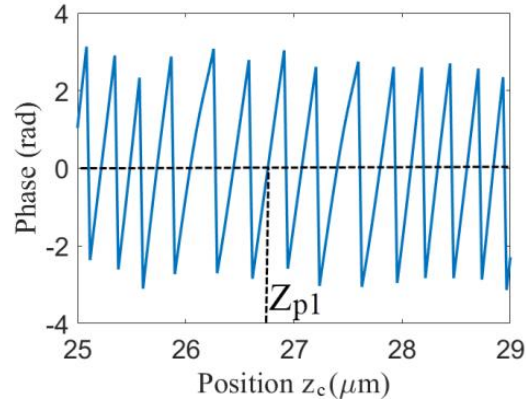


Fig. 6.7. $S_F(z_c)$ and $S_R(z_c)$ in the corrected interference signal $S(z_c)$.

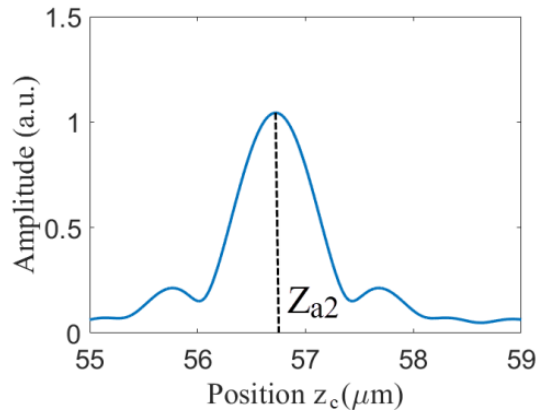
6.3.2 Signal processing

The signal processing shown in Fig. 6.2 was performed on the $S(z_c)$ to obtain the CVIS of $S_F(z_c)$ and $S_R(z_c)$. In the experiments the phase distribution in Fourier transform of $S_F(z_c)$ has a non-linear component because of the dispersion effect caused by the BS1. A least square line in the phase distribution was used to get the CVIS of $S_F(z_c)$. The first sampling point of $S(z_c)$ was regarded to be $z_c=0$. The results are shown in Fig. 6.8. The values of Z_{a1} and Z_{p1} are 26.862 μm and 27.072 μm , respectively. The values of Z_{a2} and Z_{p2} are 56.723 μm and 56.850 μm , respectively. Thus the values of $D_a=Z_{a2} - Z_{a1}=29.846$ μm and $D_p=Z_{p2} - Z_{p1}=29.778$ μm were obtained. The value of n_j was equal to 1.05 with Eq.(6.7) and it was rounded off to be 1. Finally the value of thickness T was equal to 19.439 μm with Eq. (6.8).

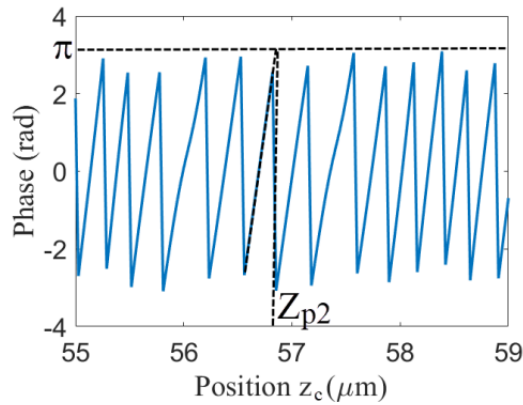




(b)



(c)



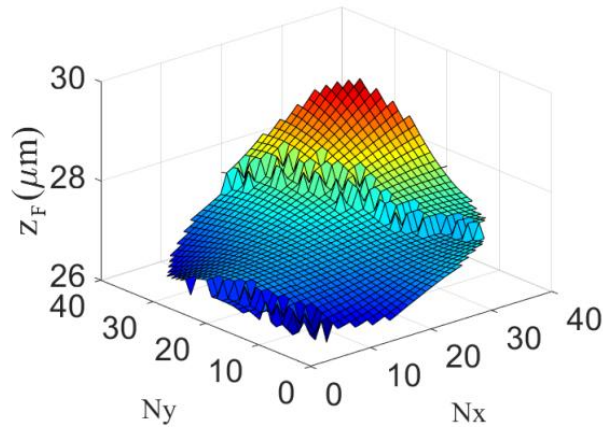
(d)

Fig. 6.8. Complex-valued interference signal of $S_F(z_c)$ and $S_R(z_c)$. (a) Amplitude and (b) phase of $S_F(z_c)$. (c) Amplitude and (d) phase of $S_R(z_c)$.

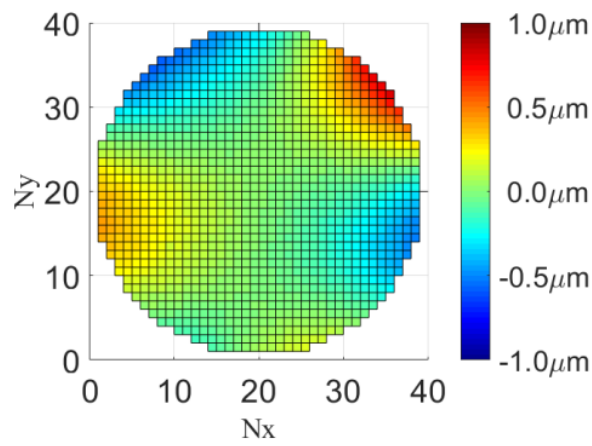
6.4 Experiment result

The shape measurement was repeated three times at intervals of about 10 minutes. These three measurements were denoted by M1, M2 and M3, respectively. Root mean square (RMS) of the difference between the two measured distributions was calculated. Average value of the three RMS

values obtained from M1, M2 and M3 was used as measurement repeatability. The signal processing in Sec.6.3 was carried out for all the measurement points to get the values of Z_{a1} , Z_{p1} , Z_{a2} , and Z_{p2} . The Z_{p1} is regarded as the front surface position Z_F as shown in Fig. 6.9(a). Since the magnitude of the dispersion phase caused by the BS1 increases linearly along the x -direction, the inclination along the x -axis and the position jump appear in the surface profile. The front surface profile after eliminating the position jumps, the inclination, and a piston component is shown in Fig. 6.9(b). The magnitude of small variation was less than 4 nm. Since air flow or mechanical vibrations caused a movement of the thin glass film, the surface profiles measured in M1, M2 and M3 were slightly different. The difference between the two surface profiles measured in MJ and M1 is denoted by MJ-M1, where $J=2, 3$. Figures 6.10 (a) and (b) show one-dimensional distributions of M2-M1 and M3-M1 at $N_x=20$ and $N_y=20$, respectively. These differences in the measured surface profiles correspond to a large measurement repeatability of 18.9 nm. The n_j values calculated with Eq. (6.7) are shown in Fig. 6.11. Since the n_j values were between 0.8 to 1.2, the value of n_j could be rounded off to be 1 over all of the measurement points. Figure 6.12 shows the thickness T distributions calculated with Eq. (6.8). The magnitude of the small variations on T distribution was less than 4 nm. Figures 6.13 (a) and (b) show one-dimensional distributions of the difference between the two measures distributions of T . Also MJ-M1 means the difference of T in the same way as Fig. 6.10. Since the thickness of thin glass film did not change the measurement repeatability of T was 2.4 nm. The $S_F(z)$ and $S_R(z)$ without the signal correction were obtained from $S_F(t)$ and $S_R(t)$ by regarding z to be $V_a t$, where V_a is the average speed of the PZT. Figure 6.14 shows one-dimensional distributions of T obtained from $S_F(z)$ and $S_R(z)$ at $N_x=20$ and at $N_y=20$. The magnitude of the small fluctuations on T distribution is less than 30 nm, and the measurement repeatability of T was 85.7 nm. It is clear that the interference signals corrected by the scanning position $z_c(t)$ provide more exact thickness measurement. Summation of a front surface profile and a thickness distribution leads to a rear surface profile. Figure 6.15 shows a profile of the rear surface in M1. The magnitude of the small variation on the rear surface was less than 4 nm.

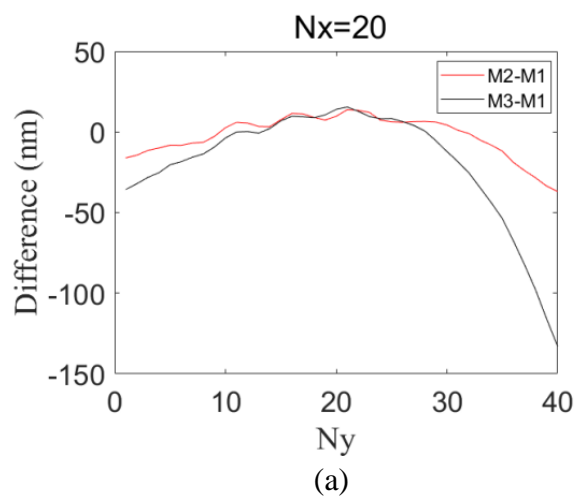


(a)

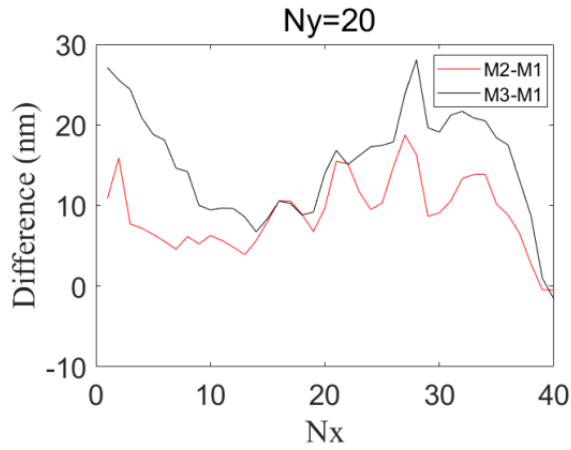


(b)

Fig. 6.9. (a) Front surface obtained from the value of Z_{p1} in M1. (b) Front surface obtained after eliminating the position jump and the inclination from (a).



(a)



(b)

Fig. 6.10. Difference M2-M1 between the two front surface profiles measured in M2 and M1, and the difference M3-M1 between those in M3 and M1. (a) at $N_x=20$ and (b) a $N_y=20$.

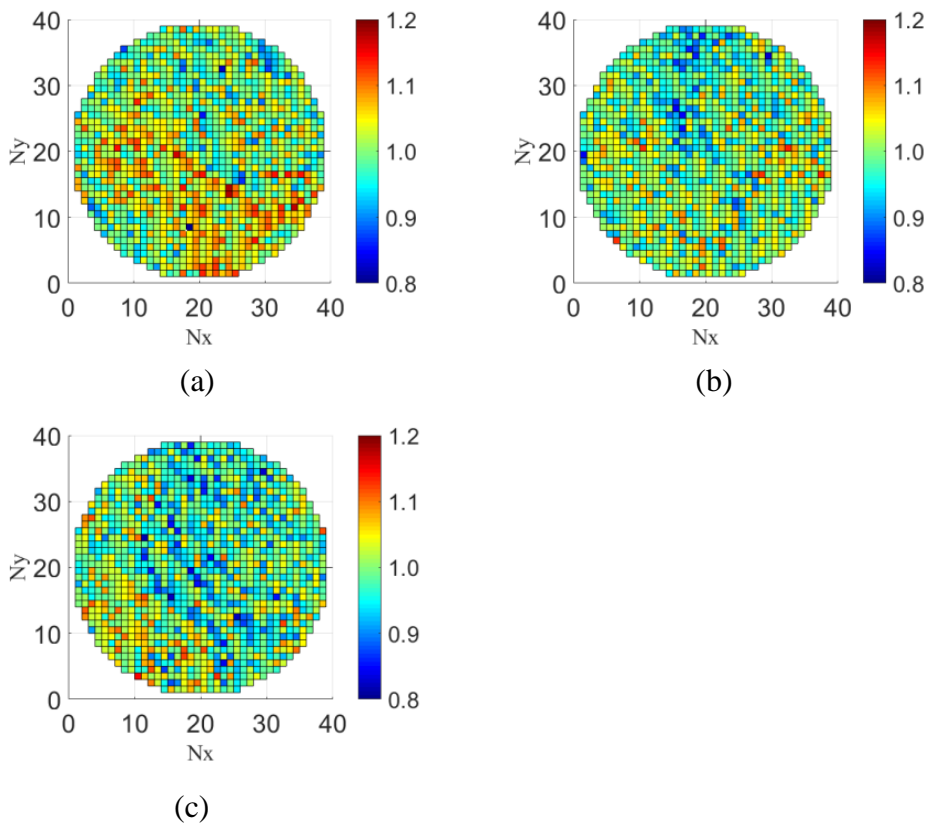


Fig. 6.11. Values of n_j obtained from $S(z_c)$ in (a) M1, (b) M2, and (c) M3.

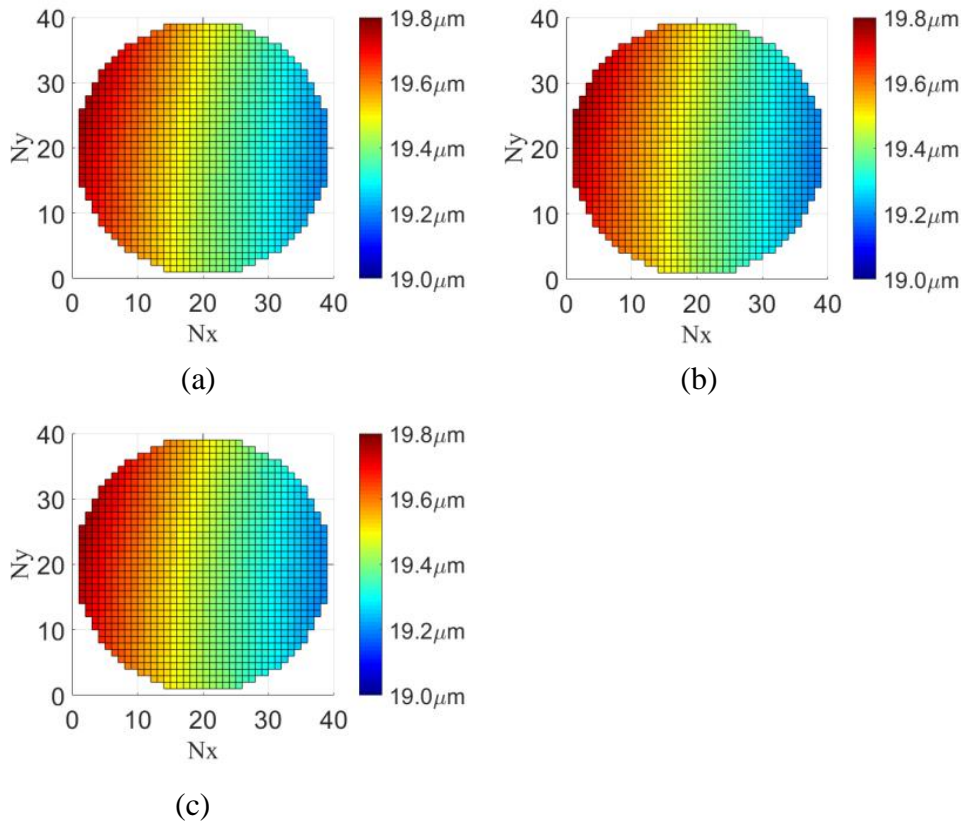
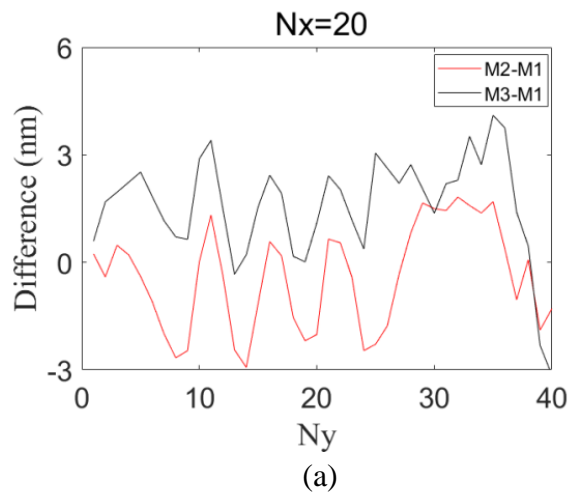
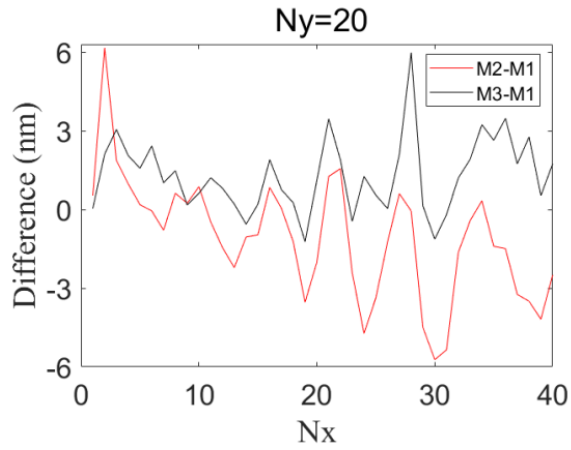


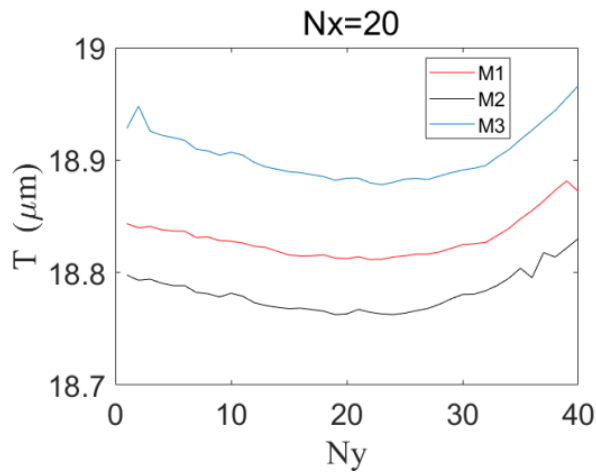
Fig. 6.12. Distribution of thickness T obtained from $S(z_c)$ in (a) M1, (b) M2, and (c) M3.



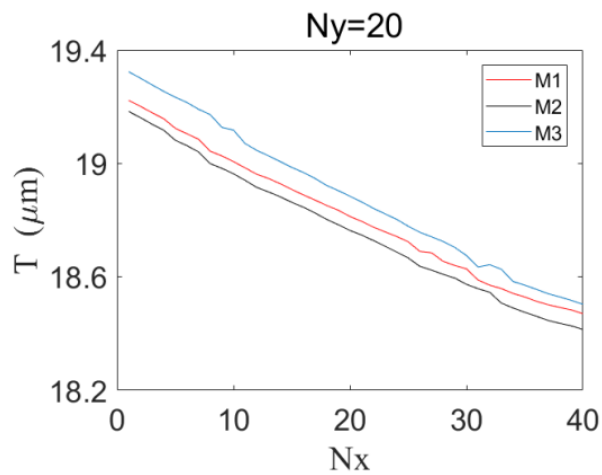


(b)

Fig. 6.13. Difference M2-M1 between the two T distributions measured in M2 and M1, and the difference M3-M1 between those in M3 and M1. (a) at $N_x=20$ and (b) a $N_y=20$.



(a)



(b)

Fig. 6.14. One-dimensional distribution of T at (a) $N_x=20$ and (b) $N_y=20$ obtained from $S(z)$.

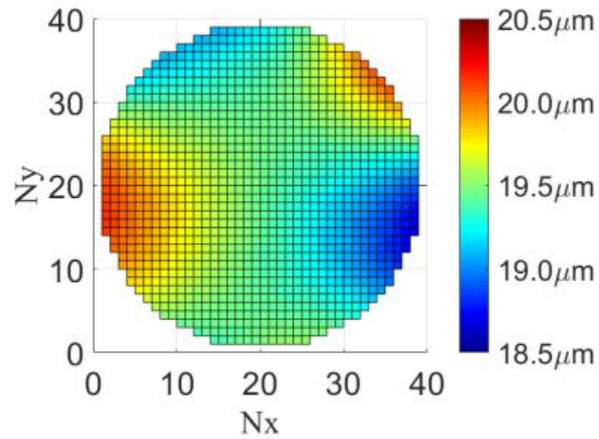


Fig. 6.15. Profile of the rear surface obtained from $S(z_c)$ in M1.

6.5 Conclusion

It has been made clear that the dispersion phase caused by thickness T of the thin glass plate produces the measurement value of $Z_a=T/C_a$ and $Z_p=T/C_p$. Also the position jump in Z_p was investigated, and the number n_j of occurrences of the position jump could be calculated from the Z_a and Z_p values. The shape measurement of the thin glass plate was achieved by using the n_j value and the constant coefficients C_a and C_p . The interference signal corrected by the detected scanning position provides an exact thickness distribution with a measurement error less than 4 nm. Although the front surface profile changed a little with time, the measurement error was less than 4 nm. These measurement errors enabled an exact shape measurement of the glass plate with about 20 μm -thickness.

CHAPTER 7

CONCLUSIONS

The purpose of researches is to improve the measurement accuracy of white-light scanning interferometer (WLSI). The dispersion phase caused by the optical component in WLSI such as the BS affects the measurement accuracy. And the random noise such as the vibration also has a bad influence on measurement. In this dissertation, a serial of methods are proposed to eliminate the dispersion phase and random noise.

The conclusion of research in this dissertation is as follow:

(1) The conventional methods to obtain the object position Z_o such as the envelop peak, intensity peak and slope of phase distribution in wavenumber domain are introduced in the chapter 1. Chapter 2 describes the process how to obtain the complex-valued interference signal. The Z_a is the envelop peak of amplitude and the Z_p is the phase zero position nearest to Z_a in complex-valued interference signal. A value of Z_p obtained from complex-valued interference signal is proposed as the new measurement value.

(2) A spectrally resolved interferometer (SRI) was used to detect the dispersion phase generated by the two sides of unequal length in beam-splitter (BS). And it was shown by the experiments that the magnitude of the dispersion phase changed linearly along the horizontal direction of the beam-splitter. The dispersion phase with a different magnitude was subtracted from the spectral phase in Fourier transform of the real interference signal of the WLSI. The dispersion-free CVIS was obtained through inverse Fourier transform of this spectral distribution, and the position Z_p provided an accurate surface profile with an error less than 4 nm after the $\lambda_A/2$ position jump correction.

(3) In order to simplify the experiment, a news signal processing is proposed in which the dispersion phase is not subtracted from the detected spectral phase distribution. The linear and bias components in the spectral phase distribution are used to calculate the complex-valued interference signal. A simulation is carried out to verify that the dispersion phase generates an inclination in the measured surface profile along horizontal direction. The simulations also show the random phase noise changes the slope of the linear component, but the position of zero phase nearest to the position of amplitude maximum in the CVSI almost does not change due to the bias component. These characteristics lead to a high accurate measurement by the new signal processing without using the dispersion phase measured with a spectrally resolved interferometer.

(4) The noise caused by the vibration of optical component and the non-linear movement of PZT change the optical path difference (OPD) in the WLSI. Two interfering beams in the WLSI can be utilized to detect the time-varying OPD. A beam-splitter is put in front of a camera for the WLSI in order to divide the two beams of the WLSI for the laser interferometer, and an optical band-pass filter is put in front of a photodiode to detect the signal of the laser interferometer. The time-varying OPD or the scanning positions can be easily and exactly obtained from this interference signal. The calculated scanning positions are assigned to the corresponding sampling points of the interference signal detected in the WLSI. This correction method for the scanning position leads to elimination of the non-constant movement of the PZT completely and the random noise caused by the external disturbances. In experiments a surface profile with a step shape of 3 μm -height is measured accurately with an error less than 2 nm.

(5) The changing dispersion phase of BS along x direction generates the $\lambda_A/2$ position jumps on value of Z_p . After the eliminating the $\lambda_A/2$ position jumps, the inclination and bias does not have influence on the surface measurement. The inclination and bias after eliminating the $\lambda_A/2$ position jumps are important for measurement of thickness. The coefficients to relate the Z_a and Z_p values to the actual thickness are determined by simulations. The number of occurrences of this position jump is obtained from the Z_a and Z_p values. An exact thickness measurement of a thin film can be achieved by using the coefficients and the number of occurrences of the position jump.

REFERENCE

- [1] E.G. Loewen, A history of engineering metrology: K.J. Hume[J]. Precision Engineering, 1981, **3**(1):15-15.
- [2] T.R. Thomas, Trends in surface roughness[J]. International Journal of Machine Tools & Manufacture, 1998, **38**(5-6):405-411.
- [3] E. C. Teague, F. E. Scire, S. M. Baker, and S. W. Jensen, "Three-dimensional stylus profilometry," Wear, **83**(1), 1-12 (1982).
- [4] J. D. Garratt, "Applications for a wide range stylus instrument in surface metrology," Wear, **83**(1), 13-23 (1982).
- [5] J. M. Bennett and J. H. Dancy, "Stylus Profiling Instrument for Measuring Statistical Properties of Smooth Optical Surfaces," Applied Optics, **20**(10), 1785-1802 (1981).
- [6] D. G. Chetwynd, X. Liu, and S. T. Smith, "A controlled-force stylus displacement probe," Precision Engineering, **19**(2), 105-111(1996),.
- [7] J. D. Garratt and S. C. Bottomley, "Technology transfer in the development of a nano-topographic instrument," Nanotechnology, **1**(1), 38---4343 (1990).
- [8] J. D. Garratt, "Survey of displacement transducers below 50 mm," Journal of Physics E Scientific Instruments, **12**(7), 563 (2001).
- [9] J. D. Garratt, "A new stylus instrument with a wide dynamic range for use in surface metrology," Precision Engineering, **4**(3), 145-151 (1982).
- [10] J. F. Song and T. V. Vorburger, "Stylus profiling at high resolution and low force," Applied Optics, **30**(1), 42-50 (1991).
- [11] B. Snaith, M. J. Edmondst, and S. D. Probert, "Use of a profilometer for surface mapping," Precision Engineering, **3**(2), 87-90 (1981).
- [12] E. Morrison, "A prototype scanning stylus profilometer for rapid measurement of small surface areas," International Journal of Machine Tools & Manufacture, **35**(2), 325-331 (1995).
- [13] X. Liu, S.T. Smith, and D.G. Chetwynd, "Frictional forces between a diamond stylus and specimens at low load," Wear, **157**(2), 279-294 (1992).
- [14] S. R. Clarka and J. E. Greivenkamp, "Ball tip–stylus tilt correction for a stylus profilometer". Precision Engineering, **26**(4), 405-411 (2002).
- [15] V. Radhakrishnan, "Effect of stylus radius on the roughness values measured with tracing stylus instruments," Wear, **16**(5), 325-335 (1970).
- [16] E. J. Davis and K.J. Stout, "Stylus measurement techniques: A contribution to the problem of parameter variation," Wear, **83**(1), 49-60 (1982).
- [17] J. H. Bruning, D. R. Herriott, J. E. Gallagher, D. P. Rosenfeld, A. D. White, and D. J. Brangaccio, "Digital Wavefront Measuring Interferometer for Testing Optical Surfaces and Lenses," Applied Optics, **13**(11), 2693-2703 (1974).

- [18] B. Bhushan, J. C. Wyant, and C. L. Koliopoulos, "Measurement of surface topography of magnetic tapes by Mirau interferometry," *Applied Optics*, **24**(10), 1489-1497 (1985).
- [19] D. Malacara "Optical Shop Testing," *Applied Optics*, **97**(591), 454-464 (2007).
- [20] G. E. Sommargren, "Optical heterodyne profilometry," *Applied Optics*, **20**(4), 610-618 (1981).
- [21] Y. Y. Cheng and J. C. Wyant, "Two-wavelength phase shifting interferometry," *Applied Optics*, **23**(24), 4539-4543 (1984).
- [22] J. C. Wyant, "Testing Aspherics Using Two-Wavelength Holography," *Applied Optics*, **10**(9), 2113-2118 (1971).
- [23] Y. Y. Cheng and J. C. Wyant, "Multiple-wavelength phase-shifting interferometry," *Applied Optics*, **24**(6), 804-807 (1985).
- [24] B. F. Alexander and K. C. Ng, "3-D Shape measurement by active triangulation using an array of coded light stripes," *Proc. SPIE 0850, Optics, Illumination, and Image Sensing for Machine Vision II*, (12 March 1988).
- [25] B.F. Alexander, "High accuracy non-contact three dimensional shape measurement," Ph.D thesis, Monash University (1989).
- [26] J. A. Jalkio, R. C. Kim, and S. K. Case, "Three dimensional inspection using multistripe structured light," *Optical Engineering*, **24**(6), 246966 (1985).
- [27] P. Seitz, "Optical Superresolution using solid-state cameras and digital signal processing," *Optical Engineering*, **27**(7), 277535 (1988).
- [28] S. B. Grossman and R. B. Emmons, "Performance analysis and size optimization of focal planes for point-source tracking algorithm applications," *Optical Engineering*, **23**(2), 232167 (1984).
- [29] J. Schwider, R. Burow, K. E. Elssner, J. Grzanna, R. Spolaczyk, and K. Merkel, "Digital wave-front measuring interferometry: some systematic error sources," *Applied Optics*, **22**(21), 3421-3432 (1983).
- [30] P. Sandoz, R. Devillers, and A. Plata, "Unambiguous profilometry by fringe-order identification in white-light phase-shifting interferometry," *Journal of Modern Optics*, **44**(3), 519-534 (1997).
- [31] P. Sandoz, "An algorithm for profilometry by white-light phase-shifting interferometry," *Journal of Modern Optics*, **44**(8), 1545-1554 (2009).
- [32] P. Hariharan, B. F. Oreb, and T. Eiju, "Digital phase-shifting interferometry: a simple error-compensating phase calculation algorithm," *Applied Optics*, **26**(13), 2504-2506 (1987).
- [33] P. d. Groot, "Derivation of algorithms for phase-shifting interferometry using the concept of a data-sampling window," *Applied Optics*, **34**(22), 4723-4730 (1995).
- [34] M.C. Park, and S.W. Kim, "Direct quadratic polynomial fitting for fringe peak detection of white light scanning interferograms," *Optical Engineering*, **39**(4), 952-959 (2000).
- [35] A. Harasaki, J. Schmit, and J. C. Wyant, "Improved vertical-scanning

- interferometry,” *Applied Optics*, **39**(13), 2107-2115 (2000).
- [36] T. Pikálek, T. Fořt, and Z. Buchta, “Detection techniques in low-coherence interferometry and their impact on overall measurement accuracy,” *Applied Optics*, **53**(36), 8463-8470 (2014).
- [37] P. Lehmann, “Systematic effects in coherence peak and phase evaluation of signals obtained with a vertical scanning white-light Mirau interferometer,” *Proc. of SPIE* 6188, 618811 (2006).
- [38] S. S. C. Chim and G. S. Kino, “Three-dimensional image realization in interference microscopy,” *Applied Optics*, **31**(14), 2550-2553 (1992).
- [39] P. d. Groot and L. Deck, “Surface profiling by analysis of white-light interferograms in the spatial frequency domain,” *Journal of Modern Optics*, **42**(2), 389-401 (1995).
- [40] P. d. Groot, X. C. d. Lega, J. Kramer, and M. Turzhitsky, “Determination of fringe order in white-light interference microscopy,” *Applied Optics*, **41**(22), 4571-4578 (2002).
- [41] M. B. Sinclair, M. P. d. Boer, and A. D. Corwin, “Long-working-distance incoherent-light interference microscope,” *Applied Optics*, **44**(36), 7714-7721 (2005).
- [42] S. Luo, O. Sasaki, Y. Liu, X. Li, Z. Lin, and J. Pu, “Elimination of dispersion effect in white-light scanning interferometer by a spectral analyzer,” *Optical Review*. **24**(1), 27-32 (2017).
- [43] S. Luo, O. Sasaki, Z. Chen, and J. Pu, “Utilization of complex-valued signals in a white-light scanning interferometer for accurate measurement of a surface profile,” *Applied Optics*, **56**(15), 4419-4425 (2017).
- [44] S. Luo, O. Sasaki, Z. Chen, S. Choi, and J. Pu, “Exact surface profile measurement without subtracting dispersion phase through Fourier transform in a white-light scanning interferometer,” *Applied Optics*, **57**(4), 894-899 (2018).
- [45] S. Kiyono, W. Gao, S. Zhang, and T. Aramaki, “Self-calibration of a scanning white light interference microscope,” *Optical Engineering*, **39**(10), 2720–2725 (2000).
- [46] S. Kim, M. Kang, and S. Lee, “White light phase-shifting interferometry with self-compensation of PZT scanning errors,” *Proc. SPIE* **3740**, 16–19 (1999).
- [47] J. Schmit and A. Olszak, “High-precision shape measurement by white-light interferometry with real-time scanner error correction,” *Applied Optics*, **41**(28), 5943-5950 (2002).
- [48] J. Liesener, M. Davidson, P. d. Groot, X. C. d. Lega, and L. Deck, “Low coherence interferometry with scan error correction,” U.S. patent 8,902,431 B2 (Dec 2, 2014).
- [49] D. Chen, J. Schmit, and M. Novak, “Real-time scanner error correction in white light interferometry,” *Proc. SPIE* **9276**, 92760I 1-15 (2014).
- [50] A. Olszak and J. Schmit, “High-stability white-light interferometry with reference signal for real-time correction of scanning errors,” *Optical*

Engineering, **42**(1), 54–59 (2003).

[51] S. Tereschenko, P. Lehmann, L. Zellmer, and A. Brueckner-Foit, “Passive vibration compensation in scanning white-light interferometry,” *Applied Optics*, **55**(23), 6172–6182 (2016).

[52] Y. S. Ghim, H. G. Rhee, H. S. Yang and Y. W. Lee, “Thin-film thickness profile measurement using a Mirau-type low-coherence interferometer,” *Measurement Science & Technology*, **24**(7), 075002 (2013).

[53] S. Costantino and O. E. Martinez, “Wide band interferometry for thickness measurement,” *Optics Express*, **11**(8), 952-957 (2003).

[54] F. Gao, H. Muhamedsalih, and X. Qian, “Surface and thickness measurement of a transparent film using wavelength scanning interferometry,” *Optics Express*, **20**(19), 21450-21456 (2012).

[55] Z. Xu, V. Shilpiekandula1, K. Youcef-toumi, and S. F. Yoon, “White-light scanning interferometer for absolute nano-scale gap thickness measurement,” *Optics Express*, **17**(17), 15105-15117 (2009).

[56] L. Ma, T. Guo, F. Yuan, J. Zhao, X. Fu, and X. Hu, “Thick film geometric parameters measurement by white light interferometry,” *Proc. SPIE* **7507**, 75070GI 1-8 (2009).

[57] S. Luo, T. Suzuki, O. Sasaki, S. Choi, Z. Chen, and J. Pu, “Signal correction by detection of scanning position in a white-light interferometer for exact surface profile measurement,” *Applied Optics*, **58**, 3548-3554 (2019).

LIST OF PUBLICATION

Publication as the first author:

1. Songjie Luo, Samuel Choi, Osami Sasaki, Takamasa Suzuki, Ziyang Chen and Jixiong Pu. “Shape measurement of thin glass plate by considering dispersion effects in a white-light scanning interferometer”, *Optics Express* (Under review).
2. Songjie Luo, Takamasa Suzuki, Osami Sasaki, Samuel Choi, Ziyang Chen, and Jixiong Pu. “Signal correction by detection of scanning position in a white-light interferometer for exact surface profile measurement”, *Applied Optics*, 58(13), 3548-3554 (2019.)
3. Songjie Luo, Osami Sasaki, Ziyang Chen, Samuel Choi, and Jixiong Pu. “Exact surface profile measurement without subtracting dispersion phase through Fourier transform in a white-light scanning interferometer”, *Applied Optics*, 57(4), 894-899 (2018).
4. Songjie Luo, Osami Sasaki, Ziyang Chen, and Jixiong Pu. “Utilization of complex-valued signals in a white-light scanning interferometer for accurate measurement of a surface profile”, *Applied Optics*, 56(15), 4419-4425 (2017).
5. Songjie Luo, Osami Sasaki, Yongxin Liu, Xiaoyan Li, Zhili Lin, and Jixiong Pu. “Elimination of dispersion effect in a white-light scanning interferometer by using a spectral analyzer”, *Optical Review* 24(1), 27-32 (2017).
6. Songjie Luo, Osami Sasaki, Samuel Choi, Takamasa Suzuki, and Jixiong Pu. “Advanced signal processing in a white-light scanning interferometer for exact surface profile measurement”, Proc. SPIE 10819, Optical Metrology and Inspection for Industrial Applications V, 108190N (8 November 2018); doi: 10.1117/12.2502790; <https://doi.org/10.1117/12.2502790>.
7. Songjie Luo, Yongxin Liu, Osami Sasaki, and Jixiong Pu. “Signal processing in white-light scanning interferometry by Fourier transform and its application to surface profile measurements”, Proc. SPIE 10023, Optical Metrology and Inspection for Industrial Applications IV, 100230V (24

November 2016);
10.1117/12.2245880; <https://doi.org/10.1117/12.2245880>.

doi:

ACKNOWLEDGEMENT

I would like to take this opportunity to express my deep gratitude to my supervisor Prof. Takamasa Suzuki, who gives me much help on my research and life during the doctoral period in Niigata University.

I am especially to express heartfelt thanks to Prof. Osami Sasaki and A/Prof. Samuel Choi. Prof. Osami Sasaki gives me guidance on the research for five years from the Master period. A/Prof. Samuel Choi teaches me how to build the setup and write the program.

I am thankful to the Prof. Jixiong Pu of Huaqiao university in China. He provides the financial support and experimental environment for some of my researches.

I am grateful to my family members. Their encouragement and support help me finish doctoral course successfully.

Finally, I would like to thank the Niigata University. There are many fine teachers and students who give me a good impression. The financial assistance from the university helps me enjoy a good life in Japan.